UNIVERSITY OF GENOA

DEPARTMENT OF EXPERIMENTAL MEDICINE – DIMES

PhD Programme in Biotechnologies in Translational Medicine

Curriculum in Bioimaging

XXXVIII Cycle

Molecular Imaging Study of the Immune Response in Muscle Denervation: a High-Tech Study in Murine Models and Human Patients

Phd Student:
Dr. Michelle Pansecchi

Thesis Supervisor:
Prof. Carlo Martinoli

2024/2025

CONTENTS

Introduction

Background

Muscle denervation occurs in various clinical settings, including trauma, diabetic neuropathy, degenerative disc disease, alcoholic neuropathy, pernicious anemia, amyotrophic lateral sclerosis (ALS), spinal muscular atrophy, Charcot-Marie-Tooth disease (CMT) and viral infections such as poliomyelitis. The consequences of denervation-induced skeletal muscle atrophy may be severe. In disorders such as ALS and spinal muscular atrophy, skeletal muscle atrophy contributes to weakness, respiratory failure, loss of independence, and mortality. In patients with diabetic neuropathy, localized denervation of small foot muscles leads to foot deformities, a major risk factor for ulcers and amputations. However, despite the prevalence and severity of denervation-induced muscle atrophy, its molecular pathogenesis remains incompletely understood (1).

The body's response to periferal nervous system nerve damage involves multiple cell types, including axonal Schwann cells (SCs), terminal (perisynaptic) Schwann cells (tSCs), endothelial cells, and immune cells such as macrophages, neutrophils and T-cells. Schwann cells are non-myelinating glial cells that reside at the neuromuscular junction (NMJ) and perform a wide variety of roles, including maintaining NMJ structure, phagocytosing nerve debris after injury and facilitating endplate reinnervation. Macrophages are an incredibly diverse cell type; they can both stimulate and control inflammation and they have the capacity to promote nerve repair. They are known to phagocytose debris of necrotic tissue fragments, secrete growth factors, promote angiogenesis, and interact with tSCs and immune cells. Several macrophage phenotypes plays a significant role in different stages of nerve degeneration and regeneration, distinguished by differential growth factor expression, which influences the surrounding environment (2).

Despite the heterogeneity of the pathological conditions previously described, they share common features such as denervation of the neuromuscular junction (NMJ) and muscle function loss with

subsequent paralysis. Defining the role of the macrophage-mediated immune response at the level of the nerve, muscle, and NMJ across different types of peripheral nerve diseases provides a broader perspective on the overall activity of macrophages in neuromuscular disorders and may offer insights for the identification of new biomarkers and potential therapeutic targets, with potential translational applications. To date, the most well-characterized immune response model related to denervation is the one associated with traumatic nerve injury.

The macrophage response to tissue injury is highly dynamic and influenced by microenvironmental signals that drive the emergence of diverse subpopulations, phenotypes and functional profiles. In the setting of peripheral nerve injury, macrophages are key regulators of the complex cascade of events required for effective nerve regeneration and restoration of function. Within the first three days following peripheral nerve injury, resident macrophages and Schwann cells (SCs) actively clear degenerated axonal fragments and contribute to the disruption of the nerve-blood barrier. Following denervation, Schwann cells (SCs) recruit blood-derived (hematogenous) macrophages to the site of injury. Macrophage accumulation typically peaks between 3 and 7 days post-injury (3).

Peripheral nerve injury vary from simple compression (neuroapraxia) to complete rupture of the nerve (neurotmesis). Following axonal section, the distal nerve stump undergoes the so-called Wallerian degeneration, in wich axons are fragmented and myelin breaks down. Initially, myelin is removed by Schwann cells via autophagy, then clearence is improved by macrophage-mediated phagocytosis. Myelin removal is an important step for nerve regeneration since myelin contains axon growth-inhibitory proteins. Neurotrophic and growth factors are released by Schwann cells and immune cells, such as macrophages, to stimulate nerve regeneration. Macrophages undergo polarization depeding on local stimuli. In the acute phase of Wallerian degeneration, proinflammatory cytokines (TNF-α, IL-1β) contribute to the differentiation of classically activated M1 macrophages that apart phagocytosis produce proinflammatory substances and realese reactive species, such as nitric oxide; this latter damages membranes, proteins and nucleic acid, contributing to tissue degeneration. At later stages of tissue clearence and under anti-inflammatory stimuli (IL-10, IL-4), alternatively activated

M2 macrophages are found in the nerve, wich act to remove cell debris, attenuate inflammatory responses and heal wounds (4)(5).

The temporal specificity and distinct cytokine expression profiles of M1 and M2 macrophages suggest that these cells may play differentiated roles in the recovery from nerve injury (6). Within the first three days following nerve injury, perisynaptic Schwann cells (pSCs) surrounding denervated synapses recruit macrophages to phagocytose debris from degenerated axons and myelin sheaths. Macrophage density peaks approximately one week post-injury, and, in concert with the activity of pSCs, these cells support the reinnervation process by promoting angiogenesis and tissue regeneration. Current evidence suggests that macrophages may play a similar role at the neuromuscular junction (NMJ); however, the specific macrophage phenotype active at the NMJ and its functional contribution to reinnervation remain to be elucidated (7).

Hereditary motor and sensory neuropathies (HMSNs) comprise a genetically heterogeneous group of disorders characterized by progressive muscular atrophy and sensory neuropathy, primarily affecting the distal extremities.

Charcot-Marie-Tooth (CMT) disease

Charcot-Marie-Tooth (CMT) disease constitutes the most common form of inherited peripheral neuropathy (8). Charcot-Marie-Tooth (CMT) disease exhibits considerable genetic heterogeneity, with documented modes of inheritance including autosomal dominant, autosomal recessive, X-linked recessive, and, in rare instances, X-linked dominant transmission (9). The most frequently implicated genes in Charcot-Marie-Tooth (CMT) disease are three myelin-related genes: *PMP22*, *P0*, and *Cx32*. The most common demyelinating subtype, CMT1A, is caused by a 1.5-Mb genomic duplication on chromosome 17 that includes the peripheral myelin protein 22 gene (*PMP22)*. This gene duplication leads to *PMP22* overexpression, which in turn results in peripheral nervous system (PNS) demyelination, as evidenced by reduced nerve conduction velocities and segmental demyelination observed in nerve biopsies (10). Less commonly, CMT1 is caused by point mutations in

the *PMP22* gene or in the gene encoding myelin protein zero (*MPZ*), the latter associated with the CMT1B subtype (11) (12,13).

CMTX1 is the second most prevalent form of Charcot-Marie-Tooth disease and is caused by mutations in the gap-junction B1 (GJB1) gene, which encodes connexin 32.

CMT2 is characterized by a highly heterogeneous genetic profile, with no single predominant gene responsible of the disease. The most frequently involved mutated gene is mitofusin 2 (MFN2), accounting for up to 20% of CMT2 cases, followed by MPZ (approximately 5%) and then by neurofilament light chain (NEFL) (14–20).

Autosomal recessive forms tend to be more severe than autosomal dominant ones, typically have an earlier onset, and may manifest as either axonal (AR-CMT2) or demyelinating forms (CMT4).

In both cases, AR-CMT2 and CMT4, the most frequently mutated gene is GDAP1, which encodes the ganglioside-induced differentiation-associated protein-1 (21,22).

Distal hereditary motor neuropathies (dHMNs) are also genetically heterogeneous and are classified based on their mode of inheritance and the specific mutated gene involved.

Regardless of the underlying metabolic or structural defect, that may primarily affects the myelin or the axon, the final common pathway typically involves an axonal degenerative process, which, in most cases, predominantly affects the largest and longest nerve fibers (23–25).

The secondary axonal degeneration accounts for the characteristic phenotype of Charcot-Marie-Tooth (CMT) disease, marked by distal limb muscle wasting, weakness, and sensory loss, as well as a progressive spread from distal to proximal regions over time (23,26).

Clinically, Charcot-Marie-Tooth (CMT) disease is characterized by a denervating process leading to slowly progressive distal muscle atrophy and weakness; motor symptoms typically begin in the feet, leading to the development of high arches (pes cavus), hammer toes, and progressive weakness and wasting of the intrinsic foot muscles. Than the disease gradually affect the legs and the thighs leading to the typical atrophy of the distal lower limbs; at the end hands and forearms are also affected. Sensory loss follows a similar pattern, primarily affecting the feet and hands. It commonly involves

reduced sensitivity to vibration, light touch, and pain. The disease typically begins within the first two decades of life and than follows a slowly progressive course over several decades. Clinical symptoms and signs suggestive of Charcot-Marie-Tooth (CMT) disease include: pes cavus (or, less commonly, pes planus that may later evolve into cavus deformity), hammer toes, difficulty in running, frequent ankle sprains or tripping, walking difficulties, foot drop, and a steppage gait. Progressive muscle wasting, weakness, and sensory loss usually start in the distal lower limbs and later involve the upper limbs, often leading to impaired hand function. Deep tendon reflex are reduced and pain is common, generally affecting feet, lower limbs and lumbar spine. Additional common signs and symptoms include hand tremors, muscle cramps (especially in the feet and legs), cold feet, foot callosities, and acrocyanosis. In more advanced stages, patients may also develop hand deformities, including the characteristic claw hand. The disorder shows a tendency to affect mutiple members of the same family (11) (27) (28).

CMT1A, caused by a duplication of the *PMP22* gene on chromosome 17p11.2, represents the most extensively characterized and prevalent subtype of Charcot-Marie-Tooth disease. Some patients with CMT1A present with delayed motor milestones, such as severe skeletal deformities proximal muscle weakness, and may require walking aids or, in rare cases, become wheelchair-bound; in contrast, others remain nearly asymptomatic and lead a normal or near-normal life. Symptoms typically begin in childhood or adolescence, with early signs including pes cavus or pes planus, areflexia in the lower limbs, and wasting and weakness of the intrinsic foot muscles, followed by involvement of the peroneal and anterior tibialis muscles.

In many cases, subtle hand involvement is also present from the early stages. Motor impairment and disability generally progress slowly over time. Clinical impairment and disability are closely associated with secondary axonal loss, as evidenced by reduced compound muscle action potential amplitudes and alterations in motor unit number estimation. (29–37)

Charcot-Marie-Tooth (CMT) disease is broadly classified into two main types: the demyelinating form, designated as CMT1 when inherited in an autosomal dominant pattern and CMT4 when

autosomal recessive. This form is characterized by significantly reduced nerve conduction velocities (typically <38 m/s in upper limb motor nerves) and marked myelin abnormalities.

The second one is the axonal form (CMT2), which presents with relatively preserved or only mildly reduced nerve conduction velocities (>38 m/s) and pathological evidence of chronic axonal degeneration and regeneration. Intermediate forms between CMT1 and CMT2 have been identified, the most prominent is the X-linked CMT (CMTX1). In addition, rare dominant-intermediate (DI) forms of CMT have been described.

Some patients with mutations in genes typically associated with either CMT1 or CMT2 may present with mixed phenotypic features, reflecting overlap between demyelinating and axonal characteristics.

A third, smaller group consists of the pure motor forms, also known as distal hereditary motor neuropathies (dHMN), which are characterized by the absence of sensory involvement on clinical, electrophysiological, and pathological examination.

The Charcot-Marie-Tooth (CMT) phenotype may sometimes be complicated by additional features, such as pyramidal involvement in HMSN type V (CMT5) or optic atrophy in HMSN type VI (CMT6). The term CMT3 (HMSN III) is occasionally used to refer to Déjèrine-Sottas neuropathy, historically described as a severe, early-onset hereditary neuropathy characterized by motor delay, profoundly reduced nerve conduction velocities, elevated cerebrospinal fluid protein levels, nerve hypertrophy, and severe dysmyelination on nerve biopsy, considered as the most severe form of demyelinating CMT (14,15,23,26).

According to some studies, even in these hereditary conditions, an endoneurial infiltration of macrophages between individual nerve fibers can be observed. This infiltration appears to contribute detrimentally to the progression of peripheral neuropathy by exacerbating clinical symptoms and accelerating the denervation process (23).

The diagnostic workup for Charcot-Marie-Tooth (CMT) subtype identification is inherently complex and cannot rely solely on clinical phenotype, as multiple genetic variants often produce overlapping clinical features, rendering them clinically indistinguishable in individual patients.

Clinical and laboratory findings as well as electrophysiological studies are essential in guiding molecular investigations, allowing for more targeted genetic testing and helping to narrow down the CMT subtypes.
Therefore, in addition to establishing the mode of inheritance, performing nerve conduction studies, and conducting nerve biopsy in selected cases, a thorough clinical examination of both the patient and affected family members may provide additional diagnostic clues (38) (15,39–42).
Magnetic Resonance Imaging (MRI) and ultrasound are two imaging modalities that provide valuable additional informations in the diagnostic evaluation of patients with Charcot-Marie-Tooth disease, particularly in detecting structural and pathological changes in nerves and muscles (43–45).

Amyotrophic lateral sclerosis (ALS)

Amyotrophic lateral sclerosis (ALS) is a progressive, devastating neurodegenerative disorder that affect both upper and lower motor neurons; it is characterized by progressive muscle weakness, atrophy, fasciculations and paralysis. Fasciculations are a prominent and diagnostic feature of ALS, resulting from ectopic activity originating within motor neurons. Evidence suggests that these fasciculations arise proximally during the early stages of the disease and shift to a more distal origin in later stages. In ALS, fasciculation potentials (FPs) are detectable from the earliest clinical stages of the disease, even in muscles that retain normal strength. However, they tend to become less evident in end-stage, severely wasted muscles, suggesting that their origin may vary throughout the course of the disease. Mortality typically occurring within 2 to 5 years of symptom onset generally due to respiratory failure (46)(47)(48). The disease is marked by the selective degeneration of motor neurons in the central nervous system (CNS), accompanied by denervation of neuromuscular synapses in the peripheral nervous system (PNS). The underlying causes and mechanisms of motor neuron degeneration in ALS are complex and remain incompletely understood. Nearly 90% of all ALS cases occur sporadically, while the remaining 10% are familial. Among familial cases, approximately 20% are associated with one of over 160 mutations in the gene encoding the ubiquitously expressed human

superoxide dismutase 1 (SOD1), the first gene identified to be linked to ALS-related neurotoxicity. Given the wide range of genes and mutations identified in familial ALS (fALS), along with the discovery of de novo genetic alterations and various environmental factors contributing to the pathogenesis of sporadic ALS (sALS), it is now evident that ALS has a highly heterogeneous etiology. Nevertheless, these different causes ultimately converge on common pathological mechanisms, leading to similar clinical manifestations (46). Electrophysiological changes are among the first measurable alterations to occur in ALS and form a major component of the diagnostic tests used in humans, as outlined in the (modified) El Escorial criteria. Alongside the Awaji criteria, these provide electrophysiological data which, when combined with the ALS Functional Rating Scale, contribute to a more definitive diagnosis. Nerve conduction measurements, such as Muscle Fiber Conduction Velocity (MFCV), have shown up to 89% effectiveness in predicting the development of ALS in patients who already exhibit denervation on muscle biopsy but do not yet meet the diagnostic thresholds of the other criteria. Altered axon excitability in ALS patients has been observed to progress in distal-to-proximal manner (46,47,49–54).

Changes in fasciculation potentials have recently been shown to precede and predict neuromuscular junction (NMJ) instability and reinnervation, consistent with an early phase of increased axonal excitability (46,48). Many studies have identified potential causes of sporadic ALS (sALS), including excitotoxicity, astroglial and/or microglial dysfunction, oxidative stress and mitochondrial dysfunction, endoplasmic reticulum stress, defects in RNA processing, growth factor abnormalities, impairments in axonal transport, metabolic alterations, and the accumulation of protein aggregates (46,55). In recent years, the 'dying-back' hypothesis has gained increasing support; this hypothesis has received considerable attention in the context of ALS pathophysiology. It suggests that pathological changes in motor neurons and nerve terminals occur before motor neuron degeneration and the onset of clinical symptoms. Specifically, it proposes that ALS is a distal axonopathy, in which changes first arise distally at the neuromuscular junction (NMJ) and then progress proximally toward the cell body (46).

The neuromuscular junction (NMJ) is a specialized structure comprising motor axon terminals, muscle fibers, and various supporting cells, including terminal Schwann cells (TSCs). Also referred to as perisynaptic Schwann cells, TSCs are glial cells localized at the NMJ and are involved in synaptic transmission, synaptogenesis, and nerve regeneration. NMJ dissociation-defined as the separation of TSCs and motor axons from the motor endplate of the muscle is a characteristic pathological feature of amyotrophic lateral sclerosis (ALS) and has been observed to precede symptom onset in both ALS rodent models and human patients. Although it remains unclear whether NMJ dissociation occurs before or after motor neuron death, accumulating evidence suggests that this process plays a more significant role in ALS progression than previously recognized.

Inflammation may contribute to NMJ dissociation during the progression of ALS, although its precise role and underlying mechanisms remain largely unclear. It is well established that inflammation is involved in motor neuron death and is associated with motor neuron degeneration within the central nervous system. As ALS advances, both pro-inflammatory and anti-inflammatory cytokine levels have been observed to increase in the cerebrospinal fluid of affected patients (56).

In both ALS patients and mouse models, motor neuron degeneration is accompanied by robust inflammatory responses. Within the central nervous system (CNS), microglia and astrocytes become activated as the disease progresses, while peripheral immune cells-such as T lymphocytes and natural killer (NK) cells infiltrate the spinal cord. The role of macrophages in the progression of amyotrophic lateral sclerosis (ALS) is complex. These cells act at both the peripheral nerve and the neuromuscular junction, where they appear to exert a protective effect during the early stages of the disease, while, in later stages, they contribute to degenerative changes. Despite the significant infiltration of macrophages observed in the peripheral nerves and muscles of *SOD1* mice, no significant alterations were detected in the expression levels of classical pro-inflammatory cytokines, including TNF-α and IL-6 (57).

The diagnosis of ALS is based on three main principles: the presence of symptoms indicating functional impairment in specific regions of the body, the evidence of both upper (central) and lower

(peripheral) motor neuron involvement in one or more anatomical regions and a progressive worsening of functional impairment over time. Electromyography (EMG) and nerve conduction studies are fundamental tools in the diagnosis of ALS; it is currently the most effective method for evaluating lower motor neuron (LMN) impairments and it plays a crucial role in early diagnosis. They not only help to distinguish ALS from other conditions that may mimic its clinical presentation but also provide evidence of motor unit loss, which is a core pathological feature of the disease.

Motor evoked potentials (MEPs) elicited by transcranial magnetic stimulation (TMS) are used to confirm lesions of the upper motor neurons (UMNs) or the corticospinal tract. In ALS, TMS typically reveals cortical hyperexcitability, characterized by an increased motor threshold and impaired intracortical inhibition, particularly a reduction in short-interval intracortical inhibition (SICI).

Advanced magnetic resonance imaging (MRI) techniques have demonstrated early degeneration of upper motor neurons, as well as involvement of other systems such as the sensory pathways and basal ganglia, supporting the view that ALS is a multisystem disorder. The use of non-conventional MRI modalities, such as diffusion tensor imaging (DTI), magnetic resonance spectroscopy (MRS), and magnetisation transfer imaging (MTI), may provide further insight into the underlying pathophysiological processes of ALS. Cerebrospinal fluid (CSF) analysis is particularly important in the early stages of the disease to exclude other neurological disorders that may mimic ALS. Ultrasound (US) has gained popularity in the assessment of neuromuscular disorders, driven by technological advancements and improved resolution. Ultrasound (US) can measure muscle size and echogenicity, as well as detect fasciculations. Given the diagnostic importance of fasciculations, and the fact that ultrasound is a quick, non-invasive, and reliable technique, especially for evaluating proximal limb and cranially innervated muscles, it is a valuable tool to use alongsidewith electromyography (EMG). The integration of these methods offers a more efficient, less invasive, and more sensitive approach to diagnose ALS (58–62) (63).

Traumatic peripheral nerve injuries (PNIs)

Traumatic peripheral nerve injuries (PNIs) encompass a range of conditions characterized by damage to one or more peripheral nerves, often resulting in partial or complete loss of motor and/or sensory function. Among the etiological factors contributing to peripheral nerve injuries, traction, transection, radiation, compression, thermal, and electrical forces are of particular relevance, as they elicit similar pathophysiological responses, including demyelination and Wallerian degeneration. Optimal functional recovery is typically achieved through early diagnosis, appropriate surgical timing (if surgical intervention is required), and the selection of the most suitable surgical approach. However, several factors can influence the outcome, including patient age, sex, comorbid conditions, the type and anatomical level of the nerve injury, as well as the presence of associated injuries (64).

Traumas represent the most common cause of peripheral nerve injuries. Among traumatic mononeuropathies of the upper extremity, the radial nerve is most commonly affected, followed by the ulnar and median nerves. In the lower extremity, the sciatic nerve is the most frequently involved, followed by the peroneal nerve. As previously mentioned neurons can be damaged through various mechanisms and the resulting pathological processes are primarily related to demyelination and Wallerian degeneration. In cases of focal demyelination, the injury remains localized without distal pathological effects. In contrast, axonal disruption leads to Wallerian degeneration of the distal nerve segment, characterized by axonal loss. In cases of traction injuries, the nerve exhibits a certain degree of resistance to the applied traction forces owing to their intrinsic tensile strength and elasticity. This tensile strength reflects the nerve's capacity to endure elongating forces. Structural adaptations contributing to this resistance include the undulating trajectory of the nerve along the limb, the wavy course of individual nerve fibers within fascicles, which provides mechanical slack, and the tensile properties of the perineurium. However, as tensile stress increases beyond physiological limits, rupture of the perineurium may occur. In case of compression injuries, the compressive strength of a nerve reflects its capacity to withstand forces that decrease its diameter. While the perineurium confers resistance to traction injury, the epineurium plays a critical role in resisting compressive

forces by dissipating externally applied pressure. Consequently, nerves with a greater amount of epineurial tissue demonstrate enhanced resistance to compression. Additionally, the fascicular architecture contributes to this resistance: a higher number of smaller fascicles more effectively dissipates compressive forces compared to a smaller number of larger fascicles. Compressive forces induce nerve injury through two primary mechanisms: direct damage to nerve fibers (axon or myelin) and the development of endoneurial edema. Endoneurial edema compromises nerve function by elevating endoneurial fluid pressure, thereby impairing axonal transport, disrupting intraneural microcirculation, and potentially leading to fibrosis. When compressive forces are brief in duration, neurological symptoms are generally transient and positive (such as paresthesia). Prolonged compression, however, may result in negative neurological features (such as numbness and weakness) due to myelin or axonal injury. In cases of transection injuries, complete or partial disruption of axonal structures, along with their associated connective tissue components, may be observed. Based on the nature of the causative force, these injuries are further categorized as either sharp or blunt. In complete transections, the proximal and distal nerve stumps often retract, forming a physical gap that significantly hinders axonal regeneration and prevents successful reinnervation of distal targets. Due to the extent of structural damage and the inherent the challenges associated with axonal regrowth, transection injuries are typically associated with a poor functional prognosis (65–67).

Two predominant classification systems have been proposed for traumatic peripheral nerve injuries: the Seddon classification and the Sunderland classification. Seddon classified peripheral nerve injuries into three categories: neurapraxia, axonotmesis, and neurotmesis.

Neurapraxia is a relatively mild form of peripheral nerve injury, characterized by temporary motor and sensory deficits without evidence of Wallerian degeneration. Distal nerve conduction remains preserved, and the conduction block is typically caused by focal demyelination and/or transient ischemia. As a condition that is largely defined by its clinical presentation, neurapraxia is associated with motor paralysis, though muscle wasting is generally minimal or absent. Electrical excitability of the affected muscles remains intact. Subjective sensory disturbances, such as numbness, tingling, and

burning sensations, are common, while objective sensory deficits are usually partial and often minimal. Loss of proprioception and vibration sense may also be present, although these findings are generally mild. Recovery typically occurs within hours to days, weeks, or up to a few months.

Axonotmesis is frequently observed in crush injuries, nerve stretch injuries (such as those resulting from motor vehicle accidents or falls), and percussion injuries (such as gunshot wounds). In axonotmesis, the axons and their myelin sheaths are disrupted, while the surrounding connective tissue structures, including Schwann cell tubes, endoneurium, and perineurium, remain preserved. Although Wallerian degeneration occurs distal to the injury site, axonal regeneration may still proceed along the preserved endoneurial tubes. The success of functional recovery largely depends on the extent of internal nerve disorganization and the distance between the lesion and the target end organ. Following a latency period of several weeks to a few months, regenerating axons may traverse the scar tissue at the injury site. If the supporting structures remain sufficiently intact, axonal regeneration can proceed in an anatomically organized manner along the distal (peripheral) stump.

Neurotmesis refers to the most severe form of peripheral nerve injury, characterized by complete transection of the nerve or profound structural disorganization due to fibrosis, which renders axonal regeneration impossible. This type of injury may result from sharp trauma, severe traction forces, high-energy blunt (percussion) trauma, or the intraneural injection of neurotoxic substances. Given the complete loss of neural continuity, the prognosis for spontaneous recovery is extremely poor in the absence of surgical intervention. At the site of nerve injury, a localized swelling known as a neuroma often develops at the proximal (central) stump; it consists in disorganized regenerating nerve fibers, fibrous scar tissue, and newly formed connective tissue. The neuroma may be palpable and tender to the touch. A similar swelling may also form at the distal (peripheral) stump. Clinically, the injury results in complete sensory loss and motor paralysis in the distribution of the affected nerve. The innervated muscles undergo denervation atrophy and exhibit the classic signs of degeneration, including the characteristic response to electrical stimulation known as the reaction of degeneration. In the absence of surgical repair, functional recovery is virtually non existent (68,69).

Sunderland proposed a more detailed classification system for peripheral nerve injuries, dividing them into five distinct degrees, in contrast to Seddon's original three-tiered model.

First-degree nerve injury corresponds to a conduction block without structural damage to the nerve's supporting connective tissue (stroma), and aligns with Seddon's classification of neurapraxia. Prognosis is excellent, as nerve function typically recovers fully.

Second-degree injury involves disruption of the axon while preserving the endoneurium and overall stromal architecture. This allows for axonal regeneration along the intact endoneurial tubes.

Third-degree injury is characterized by transection of both the axon and the endoneurial tubes, while the perineurium remains intact. Recovery depends on the ability of regenerating axons to cross the lesion site and accurately reenter appropriate endoneurial pathways.

Fourth-degree injury involves disruption of axons, endoneurial tubes, and perineurium, with only the epineurium remaining intact to maintain gross continuity of the nerve trunk. These injuries are often caused by traction forces and are associated with severe internal disorganization and fibrosis. Prognosis is poor without surgical intervention due to the lack of guidance structures for axonal regeneration.

Fifth-degree injury represents complete transection of the entire nerve trunk, including all connective tissue layers, and is functionally equivalent to neurotmesis in Seddon's classification. Surgical repair is typically required to restore any functional outcome (69,70).

A sixth degree was later added to Sunderland's classification by Mackinnon, to account for peripheral nerve injuries (PNIs) with a mixed pattern of damage (64,71).

The detection of nerve trauma is possible through neuroimaging techniques such as ultrasound (US) and magnetic resonance imaging (MRI). While electrodiagnostic tests, such as nerve conduction studies and needle electromyography (EMG), have traditionally been used for the localization and grading of nerve lesions, their utility is limited, particularly in the acute phase, and they are often poorly tolerated by patients (72)(73).

In contrast, ultrasound (US) and magnetic resonance imaging (MRI) have emerged as valuable, non-invasive complementary tools for accurately localizing and characterizing peripheral nerve injuries. Ultrasound (US) has demonstrated significant utility in improving the localization and characterization of peripheral nerve injuries and offers several advantages over magnetic resonance imaging (MRI). Specifically, US provides high spatial resolution for visualizing superficial nerves, is not affected by ferromagnetic artifacts, involves fewer contraindications related to implants, and is often better tolerated by patients. Furthermore, US is particularly well-suited for guiding perineural injections, making it a valuable tool not only for diagnostic purposes but also for the therapeutic management of painful neuropathies (73–75).

On short-axis ultrasound, peripheral nerves exhibit a characteristic honeycomb appearance, with hypoechoic fascicles surrounded by hyperechoic connective tissue (73,76).

At ultrasound examination, low-grade peripheral nerve injuries consistent with clinical and conductive neurapraxia (Sunderland grade I) may present with no detectable abnormalities on ultrasound, although mild hypoechogenicity and/or nerve swelling can occasionally be observed. Sunderland grade II injuries involve axonal damage accompanied by a more robust reparative response. These injuries may demonstrate increased edema and fascicular enlargement on ultrasound. In contrast, grade III injuries, characterized by damage to the endoneurium, often present with more pronounced, homogeneously hypoechoic nerve enlargement due to endoneural scarring. Despite this, careful imaging assessment may still reveal preserved fascicular continuity, wich correlates with a preserved perineurium. Sunderland grade II and III injuries can be difficult to differentiate on imaging; however, grade III injuries may present with focal, fusiform hypoechoic nerve swelling, commonly referred to as a pseudoneuroma. Grade IV injuries are characterized by disruption of the perineurium, leading to intraneural scarring that significantly impairs axonal regeneration. The resulting disorganized regrowth of axons, combined with fibrosis, often gives rise to a neuroma in continuity, an imaging and clinical hallmark of Sunderland grade IV nerve injury. In these lesions, nearly all internal connective tissue features become sonographically imperceptible, including a loss

of the normal fascicular architecture. However, the hyperechoic epineurium typically remains intact. In cases of neurotmesis (Sunderland grade V), sonographic imaging typically reveals complete transection of the echogenic epineurium, often with an intervening gap filled by hemorrhage or fibrosis. A stump neuroma is commonly present at the site of injury. These neuromas are identified as markedly enlarged hypoechoic nodules in continuity with the proximal or distal nerve stump and are frequently associated with tenderness, pain, or paresthesia when compressed with the ultrasound probe. Mixed-type (grade VI) injuries involve variable damage to different layers within a single nerve cross-section, with partial nerve laceration being a common example. In such injuries, some nerve segments may remain intact, while others exhibit complete transection of axons, endoneurium, perineurium, and epineurium, similar to grade V injuries. Imaging typically reveals focal thickening or discontinuity of the epineurium, accompanied by heterogeneous and disrupted fascicular patterns. Following a nerve injury, it is essential to evaluate the innervated muscle territory. Normal muscle typically appears hypoechoic with fine echogenic internal septa on ultrasound. In contrast, denervated muscle demonstrates increased echogenicity and volume loss, along with progressive effacement of the normal muscle architecture over time (73,74,76–80).

MRI is a valuable imaging modality for visualizing peripheral nerves and characterizing surrounding soft tissue structures, particularly when assessing atypical sites of compression. It also provides critical information regarding muscle denervation and atrophy. Moreover, MRI is especially useful for evaluating nerve lesions located in anatomically complex regions that may be challenging to localize with electrodiagnostic studies or difficult to visualize with ultrasound (78).

Morphologic MR neurography has substantially expanded its clinical utility through the use of two-dimensional and three-dimensional imaging sequences, both with and without fat-suppression techniques. However, these sequences are limited by their inability to provide pathophysiological information regarding the functional integrity or axonal transport within peripheral nerves. In this context, functional MRI techniques, such as diffusion-weighted imaging (DWI) and diffusion tensor imaging (DTI), serve as valuable complementary tools for the initial evaluation of peripheral nerve

trauma and for the assessment of nerves following surgical repair. These methods provide not only detailed morphologic data but also critical functional information about the extent and severity of nerve damage. Furthermore, functional MR neurography is essential to the evaluate the functional status of affected nerves and the integrity of axonal flow. Functional MR neurography, utilizing diffusion-weighted imaging (DWI) and diffusion tensor imaging (DTI) offer valuable pathophysiological insights into both healthy and pathological peripheral nerves. Diffusion-weighted imaging (DWI) is based on the ability to detect and quantify the movement of water molecules within the extracellular space. Diffusion tensor imaging (DTI) shares the same biophysical principles as DWI but takes into account the presence of a dominant direction of water molecule movement within three-dimensional (3D) space. DTI has been particularly utilized for the evaluation of the central nervous system (CNS). Quantitative parameters derived primarily from DTI neurography enable the detection of signal intensity changes in injured peripheral nerves with greater sensitivity and specificity than morphologic MR neurography. These parameters provide crucial pathophysiological information regarding the extracellular space, fiber organization, axonal flow and myelin integrity. Functional MR neurography thus holds significant potential to enhance treatment selection, guide therapy, monitor progress, and predict outcomes in patients with peripheral nerve injuries (81).

Schwann cells play a central role in initiating many of the cellular and molecular events involved in Wallerian degeneration. At the site of nerve injury, alterations in their protein expression are crucial for supporting axonal regeneration. In the absence of axonal contact, Schwann cells undergo a phenotypic shift to a non-myelinating state, characterized by the downregulation of several key proteins, including PMP22, Krox-20, P0, and connexins. Protein synthesis is suppressed, while cellular differentiation is promoted, accompanied by the upregulation of c-Jun and the production of neurotrophic factors such as nerve growth factor (NGF) and ciliary neurotrophic factor (CNTF). These neurotrophic factors promote the generation of a population of newly differentiated Schwann cells, a process that is further supported by the protective and regenerative properties of endogenous molecules such as erythropoietin. These changes are further driven by neuregulin, as well as by

mitogenic signals released from proximal stump neurons, such as ATP. Together with acetylcholine, these factors contribute to the maturation of newly differentiated Schwann cells into a myelinating phenotype (82–90).

Schwann cells play a key role in debris clearance following nerve injury, both by performing phagocytosis themselves and by actively recruiting macrophages. This phagocytic activity is supported by the expression of the protein MAC-2, which facilitates the phagocytic capacity of Schwann cells. In addition, Schwann cells are a major source of monocyte chemoattractant protein-1 (MCP-1), a chemokine that plays a crucial role in recruiting circulating macrophages to the injury site (90–93).

Following nerve injury, macrophages are rapidly recruited to the lesion site in response to signals released by Schwann cells, a process that depends on the disruption of the blood-nerve barrier. Once at the injury site, macrophages play multiple roles: they facilitate the recovery of essential lipids, such as cholesterol, from degenerating nerve tissue, and they synthesize apolipoprotein E along with other lipoproteins. In addition, macrophages secrete various growth-promoting factors that further stimulate Schwann cell proliferation, thereby supporting nerve regeneration (90,94–98).

Schwann cells play a pivotal role in promoting axonal regeneration, primarily by serving as the main source of neurotrophic factors. These factors typically interact with tyrosine kinase receptors on neurons, leading to changes in their gene expression profiles that support and enhance the regenerative process (90).

Molecular imaging

Molecular imaging has emerged as a powerful and non-invasive approach for investigating the spatial and temporal dynamics of microinflammatory processes in vivo. This methodology allows a non-invasive visualization, characterization and quantification of biological processes at the molecular and cellular levels in living organism including humans (99).

While traditional anatomical imaging remains essential for diagnosis, surgical planning, follow up and monitoring treatment response, the field of molecular imaging is rapidly advancing and offers improvements in specificity and quantification being particularly valuable for early disease detection, targeted and personalized therapy, and earlier treatment follow-up. One of the major strengths of in vivo molecular imaging lies in its ability to characterize the molecular features of pathological tissues offering a non-invasive alternative to conventional biopsy procedures or surgical interventions. This approach enables clinicians and researchers to gather crucial biological information that can be used to individualize treatment strategies (100).

A wide range of advanced imaging modalities are now extensively employed to monitor structural, functional, and molecular alterations within pathological tissues including optical imaging, computed tomography (CT), magnetic resonance imaging (MRI), positron mission tomography (PET), single-photon emission computed tomography (SPECT) and ultrasound (101). In particular, new PET radioligands and MRI contrast agents that target molecular and cellular mediators of neuroinflammation represent powerful imaging tools for improving our understanding of disease mechanisms, progression, and therapeutic response (102).

Positron emission tomography (PET) stands out as one of the most promising tools in this field, particularly when combined with radiotracers targeting immune cells. For example, the PET tracer DPA-714, which binds to the translocator protein (TSPO) expressed in activated macrophages and microglia, enables the in vivo visualization of macrophages activation and migration. This makes it particularly suitable for studying neuroinflammatory responses in various pathological conditions, including neuromuscular disorders (103).

Magnetic resonance imaging (MRI) also plays a crucial role in molecular imaging, especially when specialized contrast agents are used. Small superparamagnetic iron oxide (SPIO) and Ultrasmall superparamagnetic iron oxide (USPIO) particles, serve as effective MRI contrast agents for tracking immune cell infiltration. These particles are phagocytosed by macrophages of the reticuloendothelial system and by tissue-resident monocytes, allowing the detection of immune cell accumulation in target tissues such as muscles and peripheral nerves (104)(105).

High-resolution ultrasound (US), while traditionally considered a purely morphological imaging technique, is gaining relevance in the context of neuromuscular disease evaluation due to its excellent accessibility, portability, and non-invasiveness. Although ultrasound does not inherently provide molecular-level data, recent advances in texture analysis and artificial intelligence (AI) have significantly enhanced its diagnostic potential. Texture analysis algorithms can extract quantitative parameters from ultrasound images that reflect underlying tissue heterogeneity, fibrosis, or degeneration. When these parameters are correlated with clinical, histological, and molecular imaging findings, ultrasound may serve as a surrogate tool for monitoring disease progression and treatment response (106)(107).

Altogether, the integration of PET, MRI, and advanced ultrasound techniques, each contributing complementary informations, offers a multiparametric imaging strategy capable of characterizing the immune landscape and neuroinflammatory changes in neuromuscular diseases. This multimodal approach not only improves our understanding of disease mechanisms but also paves the way for the identification of novel imaging biomarkers for diagnosis, prognosis, and therapeutic monitoring (101).

Objectives

The present study was carried out with the contribution of a multidisciplinary team, which collaborated in the various phases of the work, from study design to data collection and analysis. The animal studies were conducted in collaboration with the staff of the Animal Facility of the San Martino Hospital in Genoa, who provided technical support and expertise throughout the experimental procedures. While the experimental studies on animal models have been completed, patient enrollment and data collection are ongoing.

Objective 1)

In vivo and ex vivo evaluation in murine models of the dynamic of the immune response at the muscle and nerve level across three different neuromuscular disorders characterized by denervation (traumatic peripheral nerve injury, genetically inherited peripheral neuropathy, and amyotrophic lateral sclerosis).

a. Development of a multiparametric imaging protocol (microPET, MRI, and ultrasound) to be applied to murine models at defined timepoints.
b. Tissue harvesting and processing at the same timepoints used for imaging studies.
c. Histological characterization of collected tissues and correlation analysis between imaging data and pathological findings.
d. Post-acquisition fusion of functional microPET images with morphological MRI scans.

Objective 2)

To evaluate the translational feasibility of advanced imaging protocols and their associated findings from murine models to three distinct cohorts of patients affected by Charcot-Marie-Tooth disease type 1A (CMT1A), amyotrophic lateral sclerosis (ALS) and traumatic peripheral nerve injury.

a. Recruitment of patients at the IRCCS Policlinico San Martino Hospital in Genoa.
b. Clinical assessment of patients using disease-specific clinical rating scales.
c. Design and implementation of disease-specific multiparametric imaging protocols, including PET (only for ALS patients), MRI, and ultrasound, guided by findings obtained from murine models.
d. Post-acquisition fusion of functional microPET images with morphological MRI scans.

Objective 3)

Application of texture analysis techniques to ultrasound images obtained from the aforementioned patient cohorts and murine models, with the aim of extracting quantitative parameters that correlate with other imaging modalities (MRI and PET), as well as with clinical and histological data. The goal is to explore the potential of identifying disease-specific and prognostic biomarkers using ultrasound, a non-invasive, low-cost, and widely accessible technique suitable for any clinical setting.

a. Export of ultrasound data (video and static images) to external storage media.
b. Visualization and analysis of the images using offline software, including the extraction of texture analysis features.
c. Statistical evaluation of significant differences in the extracted features among the three patient groups and murine models; assessment of correlations between texture features and other clinical and instrumental parameters.

Materials and methods

Objective 1)

Four types of rodents were purchased and housed at the Animal Facility of the IRCCS Ospedale Policlinico San Martino. After obtaining the authorization from the Animal Welfare and Licensing Committee of IRCCS Ospedale Policlinico San Martino (Genoa, Italy) and the approval from the Animal Welfare Body of the Italian Ministry of Health, the experimental procedures were subsequently initiated. All experiments were conducted in accordance with the guidelines of Animal Research: Reporting of In Vivo Experiments. The animal models included the following:

1. SOD1/G93A mouse, B6SJL-Tg (SOD1*G93A)1 Gur, a well-established model of amyotrophic lateral sclerosis (ALS), characterized by high copy number expression of the mutant human SOD1 protein carrying the Gly93Ala substitution. The control group consisted of wild-type B6SJL mice.
2. SD-Tg (Pmp22) Kan rat, a model of the inherited neuropathy Charcot-Marie-Tooth disease type 1A (CMT1A).
3. MpzD61N/+ mouse, a transgenic mouse model of the inherited neuropathy Charcot-Marie-Tooth disease type 1B (CMT1B), carrying a heterozygous D61N5 mutation in the myelin protein zero (MPZ) gene.
4. C57BL/6 mouse, used as a model of traumatic peripheral nerve injury, in which a standardized nerve lesion was surgically induced

All the animal models were examined at specific time points to evaluate the disease progression:

1. n = 24 SOD1/G93A mice and n = 24 wild-type controls were assessed at 60, 90, and 120 days of age
2. n= 16 SD-Tg (Pmp22) Kan transgenic rats and n=16 wild type controls were assessed 90 and 300 days of age

3. n=16 MpzD61N/+ mice and n=16 MpzD61N/N mice along with n=16 wild-type controls were evaluated at 90 and 300 days of age
4. n = 24 C57BL/6 mice underwent focal sciatic nerve crush injury at 60 days of age under appropriate anesthesia and post-operative analgesia. Animals were evaluated at 7, 14, and 90 days after nerve injury. The contralateral (uninjured) limb was used as healthy control.

The imaging equipment used to carry out the protocol included:

1. Magnetic Resonance Imaging system 7 Tesla BioSpin MRI GmbH (Bruker, Ettlingen, Germany), located in the Animal Facility of IRCCS Ospedale Policlinico San Martino. The system is equipped with Paravision 360 software and dedicated surface and volume coils.
2. Multimodal Imaging Ultrasound System Vevo LAZR-X (FUJIFILM Visual Sonics, Toronto, Canada), equipped with a 400x linear transducer operating at 30 MHz, located in the Animal Facility of IRCCS Ospedale Policlinico San Martino.
3. MicroPET system (Albira, Bruker, USA), located in the Nuclear Medicine Department of IRCCS Ospedale Policlinico San Martino.

The PET tracer used to label the TSPO protein was synthesized at the Nuclear Medicine Department of IRCCS Ospedale Policlinico San Martino.

The superparamagnetic MRI contrast agent is used to identify inflammatory processes in various body regions; it can be purchased directly from Fujifilm exclusively for research purposes (it does not have EMA approval for general commercial use). After administration, it is necessary to wait at least 24 hours to allow the contrast agent to distribute throughout the tissues, be phagocytosed by macrophages, and accumulate mainly at sites of macrophage infiltration (109). An increase in iron content at a specific site leads to a decrease in the T2* relaxation time compared to images acquired before contrast agent administration. This change can be quantitatively measured using T2* mapping sequences.

At each time point, the murine models were subjected to a series of behavioral tests aimed at assessing their motor function:

1. Rotarod test to assess motor coordination (110)
2. Hanging Wire test to evaluate hind limb strength (maximum observation time: 180 seconds)

Each animal model is organized into groups of 8 subjects per time point, with an equal distribution of males and females. The following protocol is then applied to each group:

Day 1)

Rodents were evaluated using the aforementioned behavioral tests.

Day 2)

1. General anesthesia was induced and maintained using 1% isoflurane delivered in a 3:1 mixture of air and oxygen.
2. MRI of the lower limbs was performed using the following sequences: T2-weighted sequences with fat quantification, T2*-weighted GRE sequences, Diffusion Tensor Imaging (DTI), and T1 and T2 mapping sequences (the total scan time was approximately 45 minutes).
3. Intravenous administration via a tail vein of a superparamagnetic iron oxide contrast agent, at a dose of 0.08mL/kg.
4. Ultrasound imaging of the lower limbs was also performed.

Day 3)

1. General anesthesia was induced and maintained using 1% isoflurane delivered in a 3:1 mixture of air and oxygen
2. MRI of the lower limbs was performed using the *T2-weighted GRE* sequence* to assess contrast agent uptake (total scan time was approximately 10 minutes).

3. Whole-body microPET imaging was conducted after the administration of the [18F]-DPA-714 tracer, to detect central and peripheral neuroinflammation (total scan time was approximately 50 minutes)
4. Murine models were sacrificed by CO_2 inhalation, and tissues were harvested, including the spinal cord, bilateral sciatic nerves, and bilateral muscles of the quadriceps, hamstrings, and lower leg.
5. The harvested tissues were processed and cryopreserved for subsequent histological analyses, which include:

    - Hematoxylin and eosin staining for the morphological evaluation of muscle and nerve tissues.
    - Immunohistochemical staining to assess the presence of immune cells, using rat anti-mouse antibodies targeting

        - Myeloperoxidase (MPO)
        - CD206 (AbD Serotec, 1:200, 5 µg/mL)
        - CD86, clone PO.3 (Millipore, 1:100, 5 µg/mL)
        - CD11b (Novus Biologicals, 1:200, 5 µg/mL)

    - Prussian blue staining to verify the phagocytosis of iron oxide particles within the analyzed tissues.
    - Immunostaining using rat anti-mouse antibodies against the translocator protein (TSPO), the molecular target of the PET tracer.

Objective 2)

Three studies have been submitted to the Ethics Committee:

1. A prospective observational study for patients affected by CMT1a
2. A prospective interventional study (non-pharmacological) for patients affected by traumatic nerve injury.
3. A prospective interventional experimental study involving a pharmacological agent for patients with ALS.

Studies 1. and 2. received approval from the Regional Ethics Committee (numbers 110/2023-DB ID13005 and 177/2023-DB ID13073, respectively). Study 2) is classified as interventional, as it includes a greater number of non-invasive diagnostic procedures (such as MRI and ultrasound) than those typically performed during routine clinical monitoring of patients with traumatic nerve injury.

Study 3. involves the use of the PET tracer for neuroinflammation, [^{18}F]-DPA-714, classified as a radiopharmaceutical that is currently approved by the EMA for clinical research and has been employed in various patient populations across Europe; however, it is not authorized for general circulation or routine clinical use. The submission of an interventional clinical trial protocol involving human subjects requires the preparation of a dossier on the investigational medicinal product, known as the IMPD (Investigational Medicinal Product Dossier). Radiopharmaceuticals are fully classified as medicinal products and are therefore subject to the same regulatory requirements governing clinical trials. As specified in Regulation (EU) No 536/2014, the submission of the IMPD for the neuroinflammation PET tracer must be an integral part of the documentation to be prepared and submitted for approval by the Competent Authority (AIFA) and the Ethics Committee. The approval is preliminary and mandatory for the use of the radiopharmaceutical in human experimental studies. Therefore, a dossier was prepared containing all data related to the production process of the

investigational medicinal product, using the equipment specifically designated for radiopharmaceuticals (cyclotron/synthesizers/quality control instruments) and detailing the specific expertise of the operators and the qualified personnel of the radiopharmacy unit at IRCCS Policlinico San Martino in Genoa.

1. *Patients with CMT1a (expected number = 30)*

   Patients with a confirmed diagnosis of Charcot-Marie-Tooth disease type 1A (CMT1a), based on clinical presentation, electrophysiological findings, and genetic testing, and currently followed at IRCCS Ospedale Policlinico San Martino, were enrolled in the study. Given the chronic and slowly progressive nature of the disease, each participant underwent a single time-point clinical and instrumental assessment. Patients presenting with coexisting neurological disorders were excluded from recruitment.

   The following clinical tests are performed in all patients:

- Standard neurological examination (111)
- CMT Neuropathy Score (CMTNS) (112)
- Overall Neuropathy Limitations Scale (ONLS) (113)
- Assessment of lower limb muscle strength using the Medical Research Council (MRC) scale (114)
- Measurement of foot strength (flexion and extension) using a dynamometer (115)
- 6-Minute Walk Test (6MWT) (116)
- Berg Balance Scale (BBS) for balance evaluation (117)
- Visual Analogue Scale (VAS) for pain, fatigue, and cramps (118)

All patients underwent MRI examination on the same day as their clinical visit, using a 3T Siemens Prisma scanner (Siemens Healthcare, Erlangen, Germany) located in the Neuroradiology Department of IRCCS Ospedale Policlinico San Martino. The scanning protocol, lasting approximately 50 minutes, included imaging of the hip and thighs regions. The following MRI protocol with the subsequent sequences was employed:

- T2 DIXON for the assessment of fat fraction (FF) in muscle and nerve tissue.

The Dixon sequence is a quantitative MRI technique used to assess the water–fat ratio within tissues. It relies on multi-echo acquisition and exploits the difference in resonance frequencies between water and fat protons to generate multiple image sets, including in-phase, opposed-phase, water-only, and fat-only reconstructions. Compared to traditional fat suppression methods, T2-weighted Dixon imaging provides more uniform fat suppression and is less susceptible to magnetic field inhomogeneities, making it especially advantageous for musculoskeletal imaging applications, increasing the detection of both soft tssues and osseous abnormalities. Unlike conventional MRI fat suppression techniques, which eliminate fat signal during image acquisition, the Dixon technique achieves fat suppression during post-processing, by separating fat and water signals based on their chemical shift differences (119,120).

- T1 mapping

T1 mapping is an MRI technique that generates a quantitative parametric map by acquiring a series of images at different longitudinal recovery times, allowing for voxel-wise calculation of the T1 relaxation time. T1 represents the time required for longitudinal magnetization to return to its equilibrium state following an inversion or saturation pulse. This parameter is influenced by several factors, including magnetic field strength, tissue temperature, water content, and phase contrast effects. Importantly, gadolinium-based contrast agents, which distribute within the intravascular and interstitial spaces, shorten T1 relaxation times, enabling contrast-enhanced T1 mapping. However,

T1 mapping can also be performed without contrast ("native T1 mapping"), which can reveal intrinsic tissue characteristics, such as water, lipid, collagen, protein, and iron content. Notably, iron deposition leads to a shortening of T1, T2, and T2* relaxation times. When both pre- and post-contrast T1 values are obtained, it is possible to calculate the extracellular volume (ECV), a quantitative biomarker of fibrosis and edema (121–128).

- T2 mapping

T2 mapping is an MRI technique that produces a quantitative parametric map by acquiring a series of images at different transverse decay times, allowing voxel-wise calculation of the T2 relaxation time. T2 represents the time required for the loss of phase coherence of transverse magnetization following an excitation pulse, primarily due to spin–spin interactions. T2 values are influenced by tissue composition, particularly water content, with higher T2 values typically observed in water-rich tissues. Additionally, superparamagnetic substances such as iron and deoxyhemoglobin generate local magnetic field inhomogeneities, which further reduce T2 values, more prominently affecting T2* than true T2. T2 mapping can be performed using two main sequence types, the spin-echo sequence which measure true T2 relaxation times and gradient-echo sequence which measure T2*. T2 mapping is particularly valuable for detecting pathological changes associated with fluid accumulation, such as edema and inflammation, which typically present with prolonged T2 values. Conversely, T2* mapping is well suited for evaluating conditions involving magnetic susceptibility effects, such as hemorrhage or iron deposition (129–136).

- Diffusion Tensor Imaging (DTI)

Diffusion-weighted imaging (DWI) is an MRI technique that captures the random motion of water molecules within biological tissues, enabling the generation of images based on the diffusivity differences among various tissue types. In the context of the peripheral nervous system, the highly organized structure of nerves facilitates preferential diffusion of water molecules along the

longitudinal axis of the nerve fibers, while diffusion across the perpendicular axis is more restricted. This directional preference in water movement, known as anisotropy, is a key characteristic that distinguishes nerve tissue from the surrounding isotropic tissues, where water diffuses equally in all directions. Exploiting this property, diffusion tensor imaging (DTI) extends DWI by modeling the directionality of diffusion, allowing for the visualization and quantitative assessment of nerve integrity and architecture. Diffusion Tensor Imaging (DTI) provides valuable quantitative information on both normal and pathological peripheral nerves through several key biomarkers, including fractional anisotropy (FA), mean diffusivity (MD), axial diffusivity (AD), and radial diffusivity (RD). Among these, FA is the most significant parameter, as it reflects the degree of directional organization of nerve fibers, with values ranging from 0 (completely isotropic diffusion) to 1 (fully anisotropic diffusion). FA is a highly sensitive marker of microstructural integrity and typically shows reduced values in most forms of primary and secondary neuropathies. Mean diffusivity (MD) measures the average displacement of water molecules within the extracellular space. Axial diffusivity (AD) reflects water movement along the primary axis of the nerve fiber, and is closely associated with axonal transport and axonal integrity. In contrast, radial diffusivity (RD) measures diffusion perpendicular to the main nerve axis, and is strongly related to the integrity of the myelin sheath (137–142).

The superparamagnetic contrast agent was not administered because studies on murine models demonstrated its ineffectiveness in identifying immune activation. However, the adopted protocol compensates for the absence of contrast agent by indirectly assessing damage induced by inflammatory cells in muscle and nerve tissue. The same study protocol is also applied to patients undergoing MRI of the pelvis and thigh for non-neurological issues, who serve as the control group. This control group is matched for mean age and has a similar proportion of males and females. For both patients and the control group, after image acquisition, each parameter was independently assessed by two radiologists to evaluate interobserver agreement.

On the same day as the MRI, patients also underwent ultrasound evaluation.

2. *Patients with traumatic nerve injury (expected number = 20)*

Patients with traumatic nerve injury, including neurotmesis and all degrees of axonotmesis, affecting either the upper or lower limb, are enrolled within 15 days of the traumatic event while receiving care at IRCCS Ospedale Policlinico San Martino.

DAYS SINCE TRAUMA	0-14	15	30	90	180
CLINICAL ASSESSEMENT	x	x	x	x	x
QUESTIONNAIRES		x	x	x	x
IMAGING (MRI, US)		x	x	x	
ELECTRONEUROGRAPHY (ENG) ELECTROMYOGRAPHY (EMG)		x		x	

Table 1. Assessement performed on patients and their corresponding time points.

1. The clinical visit includes the following assessments:

- Segmental strength testing of the affected limb, graded from 0 to 5 according to the Medical Research Council (MRC) Manual Muscle Testing scale
- Sensory evaluation of the affected limb, assessing pain, light touch, temperature, vibration, and proprioception
- Deep tendon reflexes, graded from 0 to 4+

The questionnaires used are:

- Disabilities of the Arm, Shoulder and Hand (DASH) for patients with superior arm lesions (143)
- 36-Item Short Form Survey (SF-36) for patients with superior arm lesions

2. MRI examinations are performed using a 3T Siemens Prisma system (Siemens Healthcare, Erlangen, Germany) located in the Neuroradiology Department of IRCCS Ospedale Policlinico San Martino. Both the affected limb and the contralateral healthy limb, serving as a control, are scanned.
   The MRI protocol is the same as that used for CMT1a patients.
3. Patients also undergo ultrasound evaluation on the same day as the MRI examination.
4. Electrophysiological studies include:
   - Nerve conduction studies (electroneurography), assessing the amplitude of the CMAP (compound muscle action potential), motor onset latency in the target muscle, amplitude of the SNAP (sensory nerve action potential), sensory latency, and nerve conduction velocity
   - Electromyography (EMG)

3. *Patients with ALS (exptected number = 40)*

Patient enrollment will begin once a positive opinion has been obtained from the Ethics Committee and the National Competent Authority.

Objective 3)

Ultrasound images from animal models were acquired according to the previously specified timing and intruments. Rats and mice underwent ultrasound examination immediately after MRI while still anesthetized.

The ultrasound study in murine models includes:

- Acquisition of 3 static axial images (proximal thigh, mid-thigh, and proximal third of the leg) for each limb, perpendicular to the orientation of the muscle fibers
- Three transverse scan video clips of the same areas
- Export of the ultrasound images saved in bitmap format for offline analysis

All patients undergo ultrasound examination on the same day as the MRI. For this purpose, the Aplio i800 ultrasound system (Canon Medical Systems, Otawara, Japan), equipped with an 18-5 MHz linear probe, located in the Radiology Department of IRCCS Ospedale Policlinico San Martino, is used.

The ultrasound study in humans includes:

- Acquisition of 5 static axial images for each thigh, perpendicular to the orientation of the muscle fibers
- Three transverse scan video clips of the same area
- Export of the ultrasound images, which were saved in bitmap format and analyzed offline

The images are subsequently analyzed using the MaZda software, version 4.6 (Technical University of Lodz, Institute of Electronics, Lodz, Poland). For each image, a region of interest (ROI) was manually adapted to the anatomical area of interest. Within each ROI, the following features are extracted:

- First-order textural analysis parameters, such as mean pixel intensity (numerical pixel values) and heterogeneity (mean standard deviation) of the pixel intensity values
- Higher-order textural analysis parameters, including: histogram-derived features, absolute gradient (spatial variation of gray-level values), run-length matrix (gray-level values and run lengths in a given direction), co-occurrence matrix (information on the distribution of pixel pairs separated by a defined distance and direction), autoregressive model (describing the correlation between neighboring pixels), and wavelets (frequency decomposition of the image at multiple scales)

The reproducibility of the parameters obtained through texture analysis was tested by setting ROIs at different sizes and applying the Intraclass Correlation Coefficient (ICC) across multiple measurements, with statistical significance set at $P < .05$.

First-order parameters were compared between different patient groups using Student's *t*-test, or the Mann–Whitney Rank Sum test in cases of non-normal data distribution. Correlations between first-order parameters and other imaging data (MRI, PET) as well as histological findings (semiquantitative assessment of macrophage infiltration in murine tissue) were tested using simple linear regression analysis.

Higher-order parameters undergo further selection to identify those that most effectively differentiate between patient groups. This process involves one-way analysis of variance with the Games–Howell post-hoc test for continuous variables, and Fisher's exact test for categorical variables. The overall sensitivity and specificity of the texture-derived parameters will be evaluated by calculating the area under the curve (AUC) across the different groups.

Results

Objective 1)

The experimental studies and data collection on animal models have been completed. Preliminary results are presented below. Further analyses on the data already acquired will be carried out in the coming months.

SOD1/G93A Mice

Eighteen out of twenty-four mutant mice and all twenty-four control mice completed the experimental protocol. The six missing mutant mice (2 at 90 days of age and 4 at 120 days) died on day 3 of the protocol.

MRI parameters showed a statistically significant difference ($p < 0.05$) between mutant and control mice only in the 120-day-old group, and only for Fractional Anisotropy (FA) values obtained from Diffusion Tensor Imaging (DTI) sequences. These findings diverge from those reported in a similar study conducted by Riva N. et al., who investigated SOD1/G39A mutant rats. The discrepancy in results may be attributed to anatomical differences such as the larger diameter of the rat sciatic nerve compared to that of the mouse, wich enables more accurate value sampling and a better signal-to-noise ratio.

SOD1/G93A	muscle T2fws (FF%)	nerve T1(ms)	nerve T2 (ms)	FA	muscle T2* (delta pre-post contrast)
60 gg	5.34 ± 0.6	1893.23 ± 114	56.17 ± 5.17	0.48±0.03	2,8 ± 1
90 gg	5.42 ± 0.4	1906.34 ± 104	57.14 ± 4.16	0.47±0.1	2,9 ± 0.9
120gg	5.8 ± 0.3	1779.28 ± 99	55.23 ± 4.23	**0.31±0.06**	2,7 ±1

Table 2. Mean values ± standard deviation of MRI parameters in the SOD/G93A mouse model.

WILD TYPE	muscle T2fws (FF%)	nerve T1(ms)	nerve T2 (ms)	FA	muscle T2* (delta pre-post contrast)
60 gg	5.21 ± 0.7	1902.21 ± 111	55.13 ± 5.2	0.52±0.04	2,2 ± 1
90 gg	5.30 ± 0.8	1899.03 ± 103	52.12 ± 3.6	0.50±0.23	2,4 ± 0.9
120gg	5.7 ± 0.4	1820.24 ± 102	51.29 ± 4.2	**0.49±0.07**	2,1 ± 0.3

Table 3. Mean values ± standard deviation of MRI parameters in the Wild Type mouse model.

Similarly, behavioral tests revealed significant motor impairment only in the 120-day-old group, with abnormal values observed in both tests performed.

SOD1/G93A	Rotarod (s)	Hanging Wire (s)
60 gg	112.46 ± 46	180
90 gg	108.43 ± 34	175±5
120 gg	**80.34 ± 29**	**80±12**

Table 4. Mean values ± standard deviation of motor impairment in SOD1/G93A mouse model assessed by the Rotarod and Hanging wire tests.

WILDTYPE	Rotarod (s)	Hanging Wire
60 gg	111.39 ± 41	180
90 gg	110.48 ± 32	180
120 gg	**109.12 ± 22**	**180**

Table 5. Mean values ± standard deviation of motor impairment in Wild Type mice assessed by the Rotarod and Hanging wire tests.

MicroPET imaging showed tracer accumulation in the lower limb muscles of all mutant mice starting at 60 days of age, emerging as the most sensitive parameter for detecting altered muscle metabolism.

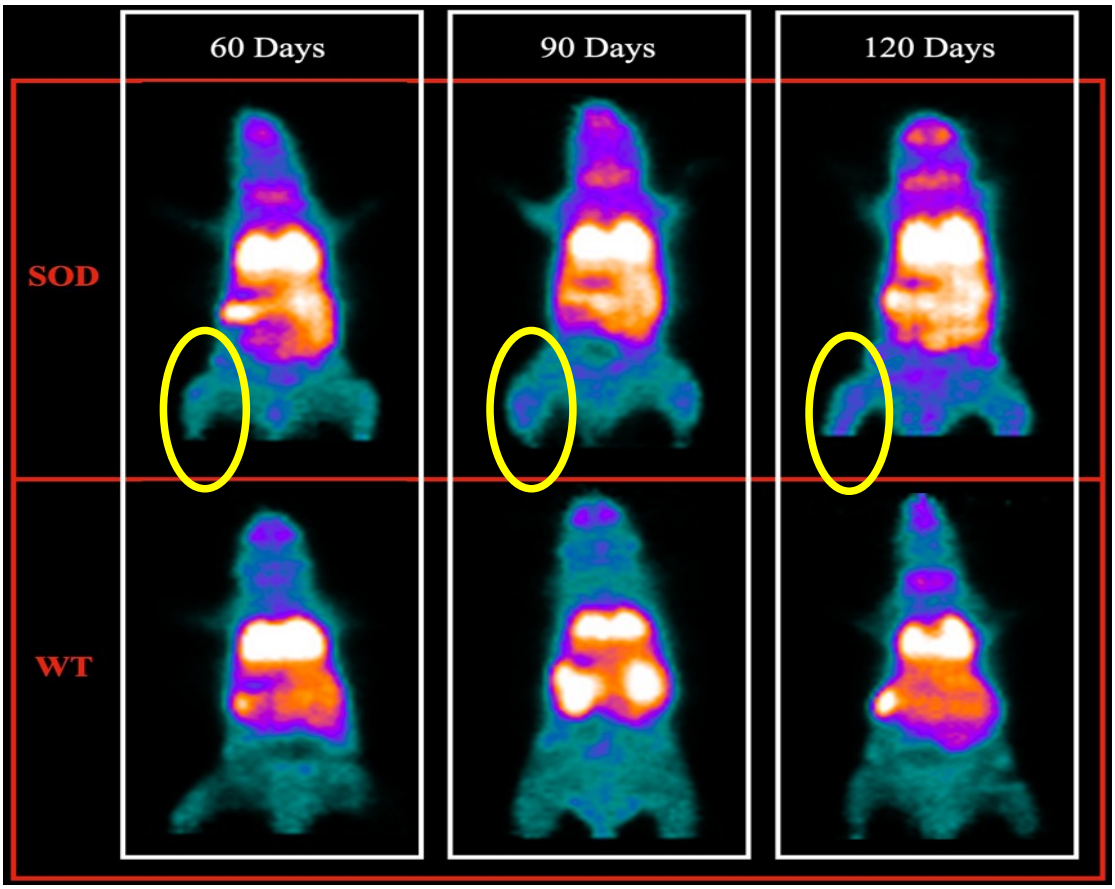

Figure 1. MicroPET images comparing the SOD1/G93A mouse model with the Wild Type. The images on the top show tracer accumulation in all mutant mice starting froma 60 days of age.

Histological analysis revealed increased expression of the TSPO protein in myocytes of mutant mice, along with a macrophage infiltrate observed by electron microscopy in the sciatic nerve.

Hematoxylin and eosin staining revealed no appreciable inflammatory infiltrates in the quadriceps muscles of either SOD1/G93A transgenic mice or their wild-type models. In contrast, a progressive atrophy of myofibers was evident in the transgenic mice compared with control animals. Moreover, nuclei within the skeletal muscle of mutant mice appeared more numerous, enlarged and positioned closer together, likely reflecting ongoing tissue degeneration. Furthermore, both muscle atrophy and nuclear alterations progressively worsened with age in SOD1/G93A mice, while remaining unchanged in the wild-type mice.

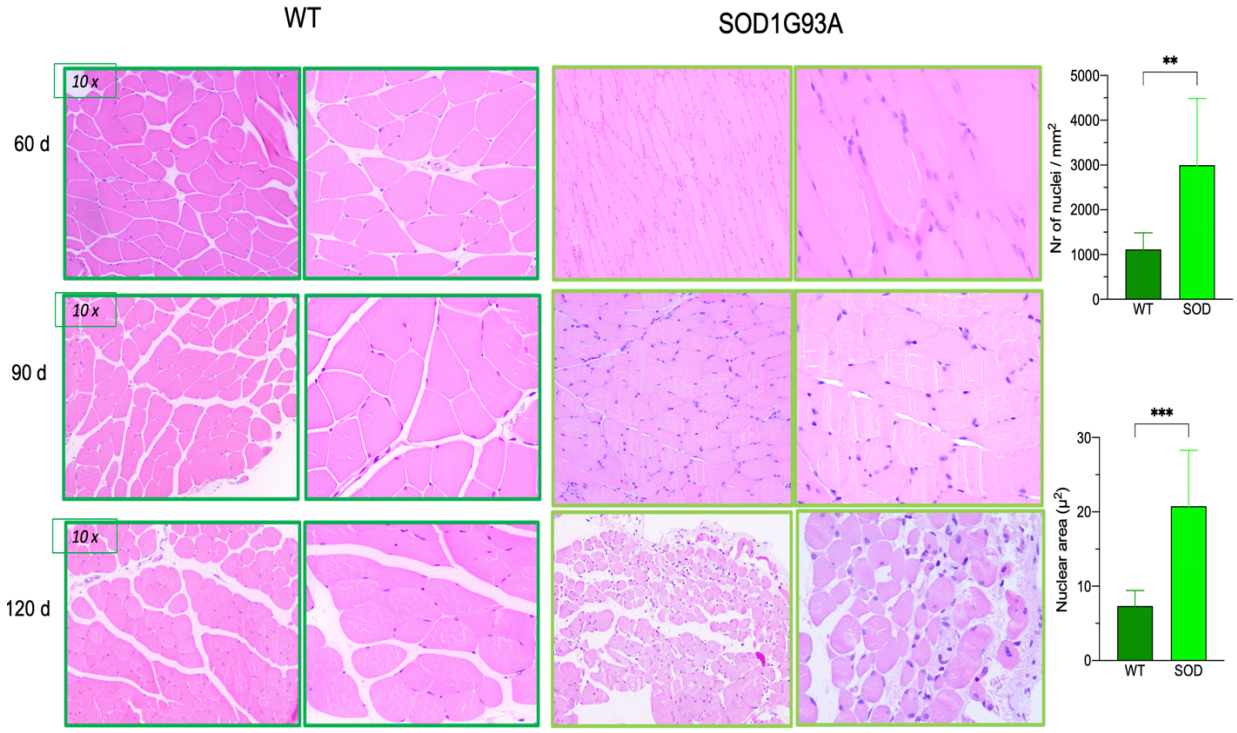

Figure 2. Hematoxylin and eosin staining of quadriceps muscle from Wild Type mice (left) and SOD1/G93A mice (right) at different ages revealed the absence of inflammatory infilitrates and a progressive atrophy of myofibers in the trangenic group.

Immunohistochemical staining using an anti-TSPO antibody (the target of the PET tracer, visualized as brown staining) revealed an age-dependent increase in TSPO expression in mutant mice.

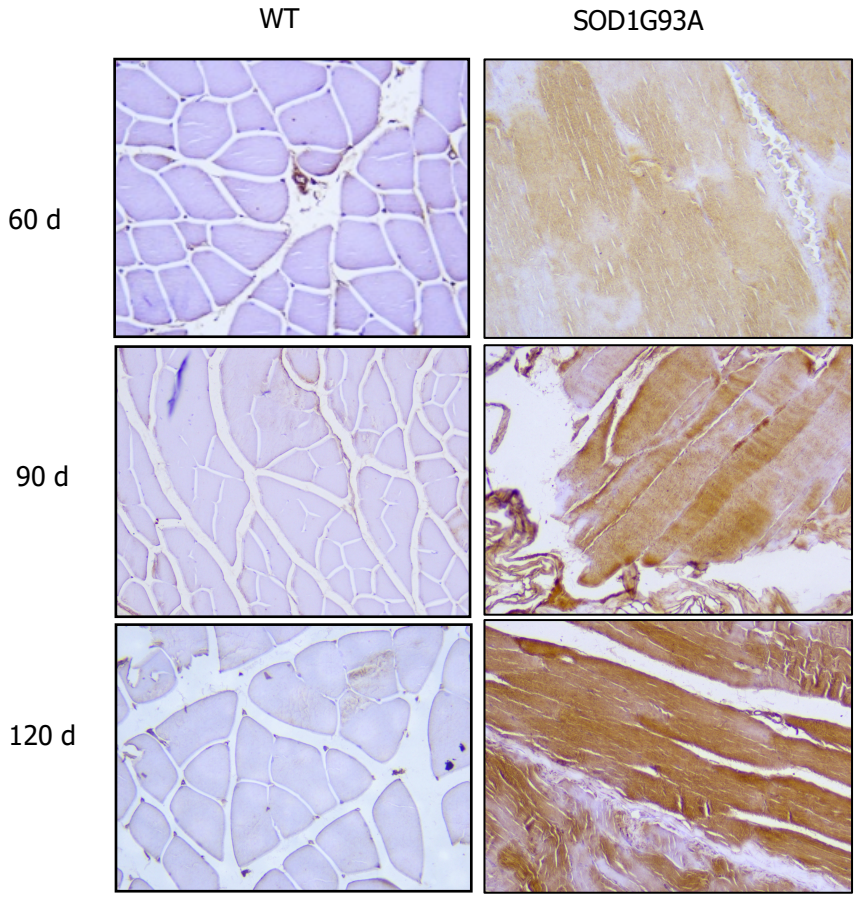

Figure 3. TSPO immunostaining of quadriceps muscle in Wild Type mice and SOD1/G93A mice at different ages. Staining was absent in Wild Type mice, whereas it progressively increased in SOD1/G93A mice.

The electron microscopy shows the presence of macrophages in the sciatic nerve of a SOD1/G93A model.

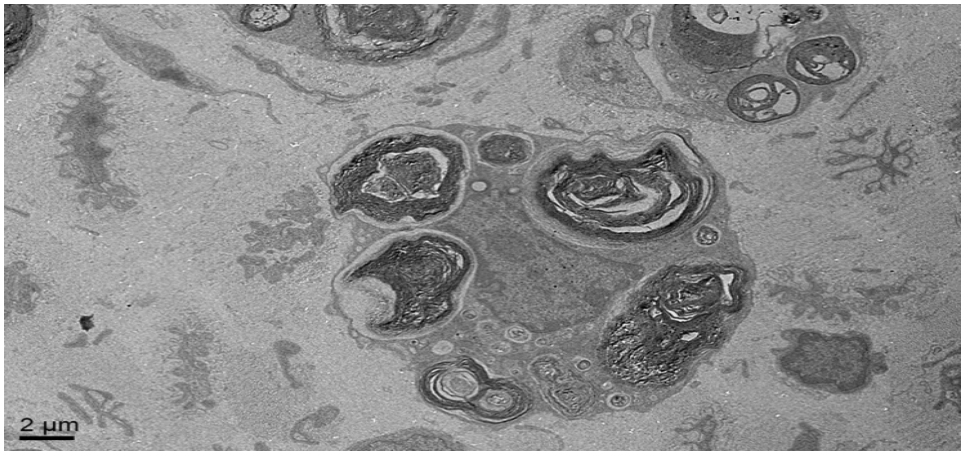

Figure 4. Electron microscopy analysis of macrophage infiltration in the sciatic nerve of SOD1/G93A mice.

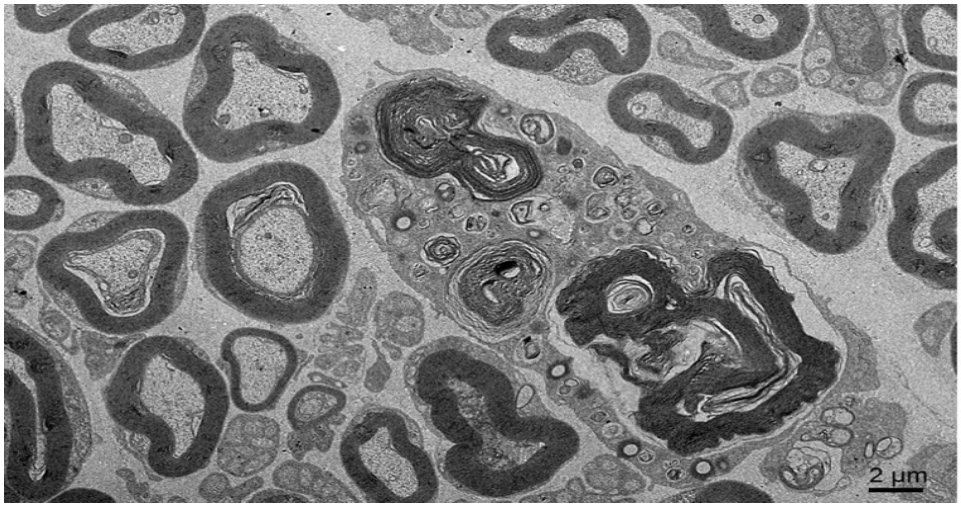

Figure 5. Electron microscopy analysis of macrophage infiltration in the sciatic nerve of SOD1/G93A mice.

CMT1A Model: SD-TG (Pmp22) Kan Transgenic Rats

Sixteen out of sixteen mutant rats and sixteen out of sixteen control rats successfully completed the experimental protocol.

MRI revealed statistically significant differences compared to controls for both Fractional Anisotropy (FA) and T1 values (derived from T1 mapping sequences) in the proximal segment of the sciatic nerve at 300 days of age ($p < 0.05$).

CMT1A	muscle T2fws (FF%)	nerve T1(ms)	nerve T2 (ms)	FA	muscle T2* (delta pre-post contrast)
90 gg	4.9 ± 0.5	1956.34 ± 102	58.23 ± 5.11	0.53±0.17	3 ± 0.34
300gg	5.2 ± 0.9	**2400.19 ± 68**	52.23 ± 4	**0.35±0.03**	2,2 ±1.2

Table 6. Mean values ± standard deviation of MRI parameters in the CMT1A mouse model.

WILD TYPE	muscle T2fws (FF%)	nerve T1 (ms)	nerve T2 (ms)	FA	muscle T2* (delta pre-post contrast)
90 gg	4.7 ± 0.4	1996.03 ± 87	55.12 ± 3.4	0.57±0.25	2,5 ± 0.5
300gg	4.9 ± 0.8	**1900.24 ± 93**	49.29 ± 4.8	**0.49±0.14**	2,6 ± 1.7

Table 7. Mean values ± standard deviation of MRI parameters in Wild Type rats.

No significant differences were observed between mutant and control rats in behavioral testing.

This finding is not in agreement with data previously reported in the literature, where mutant rats in the advanced stage of the disease show a significant decline in motor coordination at 300 days of age, as assessed by the Rotarod test (144). This discrepancy could be explained by differences in the Rotarod device used. The instrument employed in the referenced study is characterized by a larger diameter than the one available in our Animal Facility, potentially resulting in increased physical demand and stress on the animals during the tests.

MicroPET imaging did not show increased tracer uptake in muscle tissue.

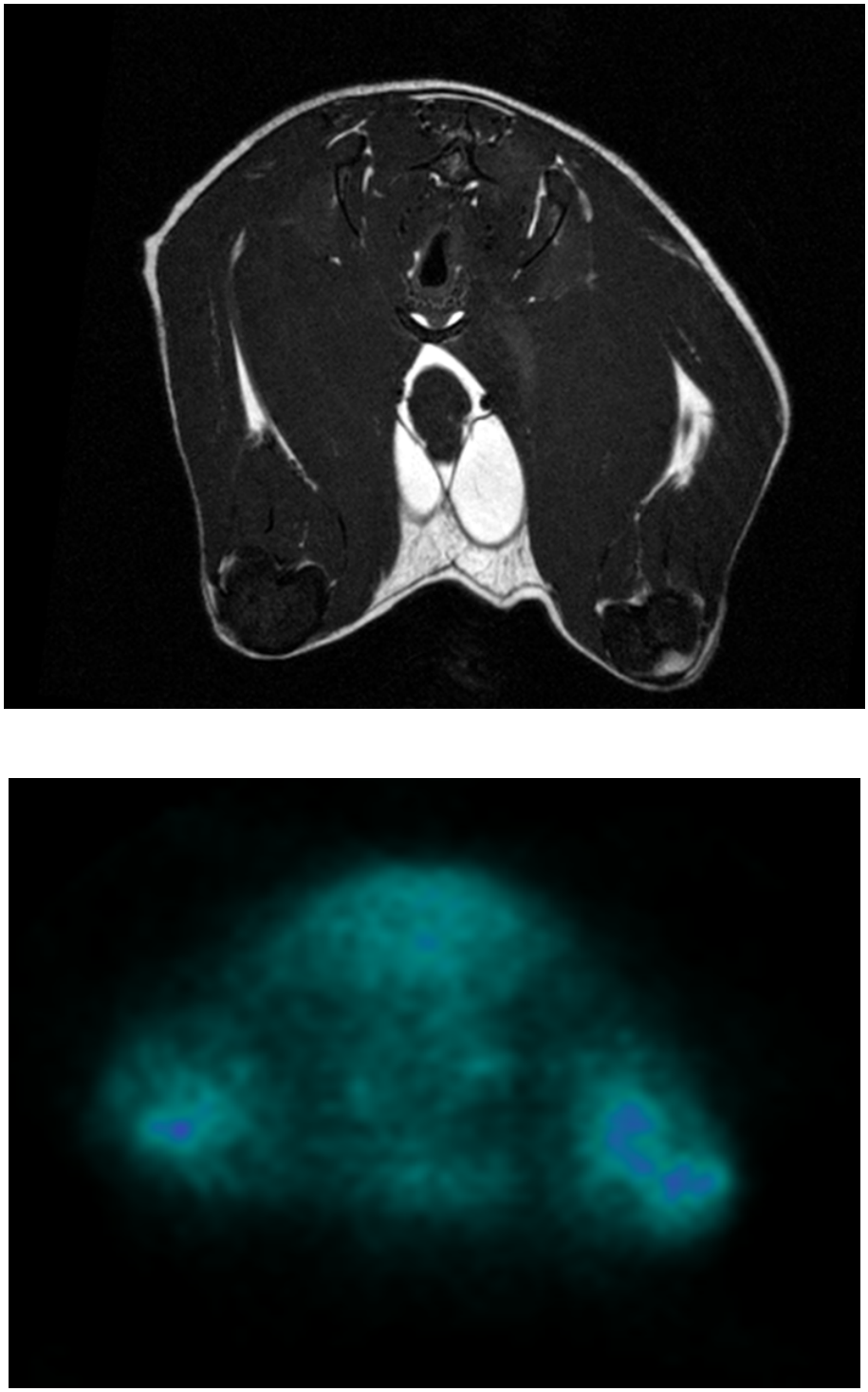

Figure 6. The images above show a morphological MRI scan (on the top) and the corresponding PET scan (on the bottom); no evidence of abnormal tracer uptake was detected in the muscles of CMT1A rats.

Histological analysis revealed pronounced structural degeneration of peripheral nerves, which became more evident at 300 days of age. This was characterized by a marked increase in intraneural collagen deposition, in the absence of any detectable inflammatory infiltrate.

CMT1B Model: MpzD61N/+ mutant mice

Sixteen out of sixteen MpzD61N/+ mice (heterozygous form), sixteen out of sixteen MpzD61N/N mice (homozygous form) and sixteen out of sixteen wild type mice were examined at 90 and 300 days of age.

Using a dedicated 7T MRI system, we aimed to evaluate the disease progression and severity, by measuring three parameters potentially linked to nerves and muscles damage:

- T1 relaxation time in the quadriceps muscle. While T1 values are often associated with fat, in muscle tissue they may also reflect changes due to edema, cellular depletion or expansion of the extracellular space
- ΔT2* in the quadriceps muscle, calculated as the difference in T2* values before and 24 hours after the administration of Ferumoxytol, a contrast agent phagocytosed by macrophages. We hypothesized that the magnitude of ΔT2* would correlate with the extent of macrophage infiltration in the tissue.
- Fractional anisotropy (FA) in the sciatic nerve is a well established marker of structural integrity.

While T1 and ΔT2* parameters remained unchanged in mutant mice, MRI analysis demonstrated a progressive reduction in fractional anisotropy (FA) values between the 90 and 300 day old mutant mouse groups ($p < 0.035$), with lower values observed in homozygous mice. FA thus appears to be a valid biomarker of disease severity.

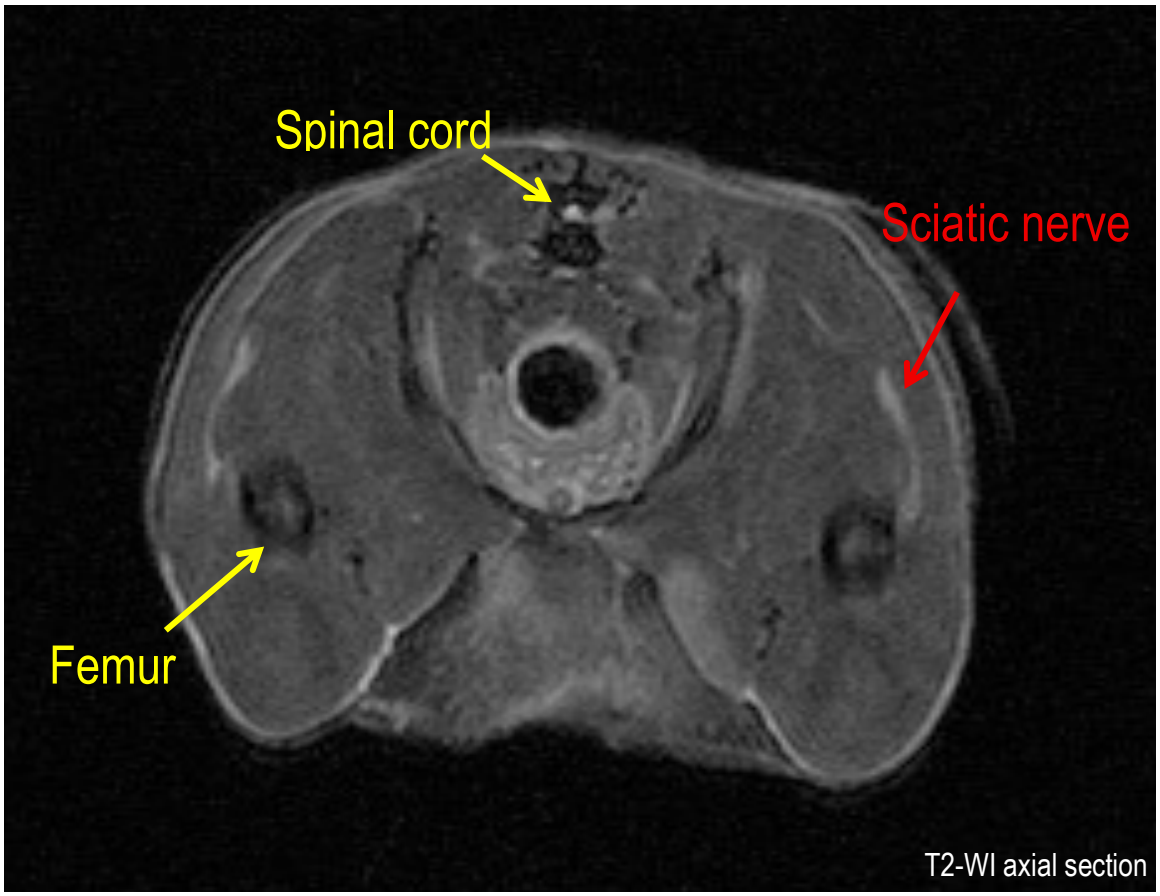

Figure 7. MRI image of an axial cross-section of the hind limbs of a mutant CMT1B mouse; the sciatic nerve is indicated by the red arrow.

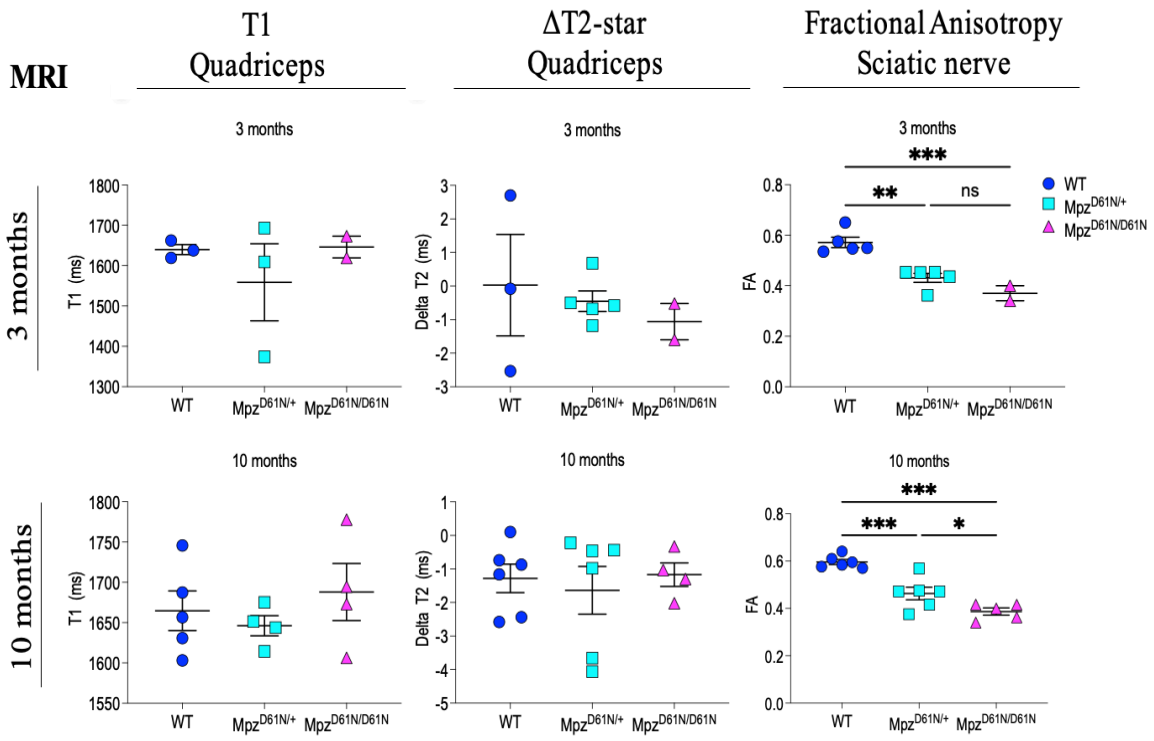

Figure 8. Graphical representation of MRI parameters, specifically T1 and ΔT2, evaluated at the level of the quadriceps muscle, and fractional anisotropy of the sciatic nerve in WT mice and CMT1B mice in the heterozygous (MPZ^D61N/+^) and homozygous (MPZ^D61N/D61N) forms.*

The translocator protein (TSPO) is highly expressed by activated macrophages. Consequently, TSPO-targeted molecular imaging has been proposed as a strategy to detect and quantify inflammation in vivo. To evalutate this approach, we assessed the accumulation of DPA-714, a TSPO-specific ligand, in regions innervated by the sciatic nerve in homozygous, heterozygous and wild type mice, using microPET imaging. The analysis revealed no differences in the standardized uptake value (SUV) between mutant and wild-type mice, suggesting the absence of significant macropaghe infiltration at the muscle level.

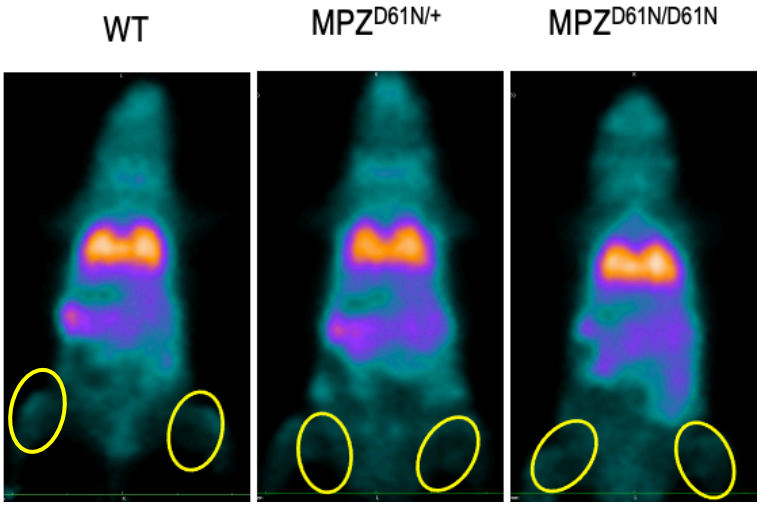

Figure 9. MicroPET images of WT, CMT1B heterozygous,and CMT1B homozygous mice showed no sign of TSPO upregulation at the muscle level.

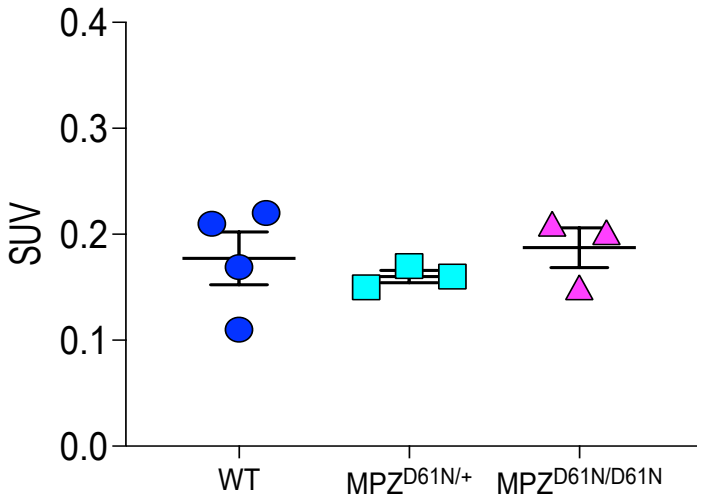

Figure 10. Graphical representation of standardized uptake value (SUV) wich remained unchanged between Wild Type and mutant mice,

At 365 days, mutant mice showed lower performance in both the Rotarod test ($p < 0.03$) and the hanging wire test ($p < 0.02$) compared to healthy controls, with homozygous mutant mice displaying the worst performance.

At 3 months of age etherozigous mutant mice showed motor performace comparable to wild-type controls, wherease the omozygous mutant mice exhibited marked coordination deficits. At 10 months of age, both etherozygous and homoygous mutant mice showed significantly impaired coordination in comparison to wild-type. These findings suggest that, while the MPZ-D61N heterozygous mutation is associated with a severe early onset neuropathy in humans, it may lead to a more gradually progressive form of the disease in rodent models.

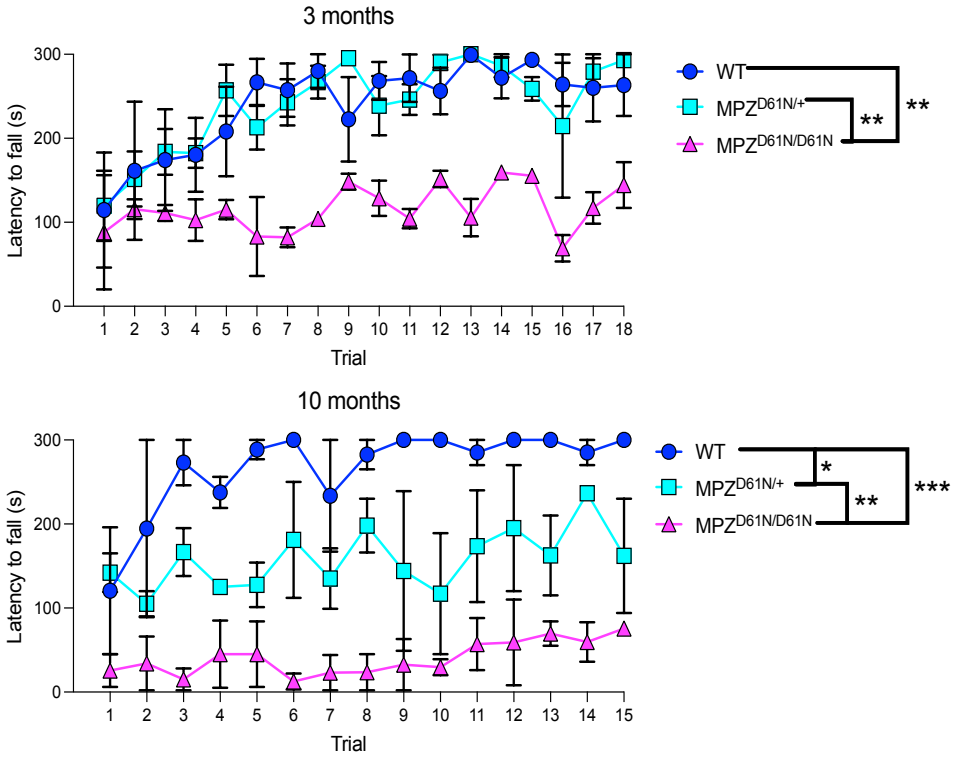

Figure 11. Graphical representation of motor performance in WT, homozygous, and heterozygous mutant mice at 3 and 10 months of age.

Histological analysis revealed disorganization of nerve fibers similar to that observed in CMT1A. To assess the inflammatory status of the sciatic nerve, we performed immunofluorescent staining for myeloperoxidase (MPO), a marker of neutrophils. We observed a marked increase in the density of MPO-positive cell in the sciatic nerve of adult homozygous mice at 300 days. This finding may suggests that the presence of a persistent inflammatory state in homozygous mice, may contribute to exacerbate the pathological phenotype.

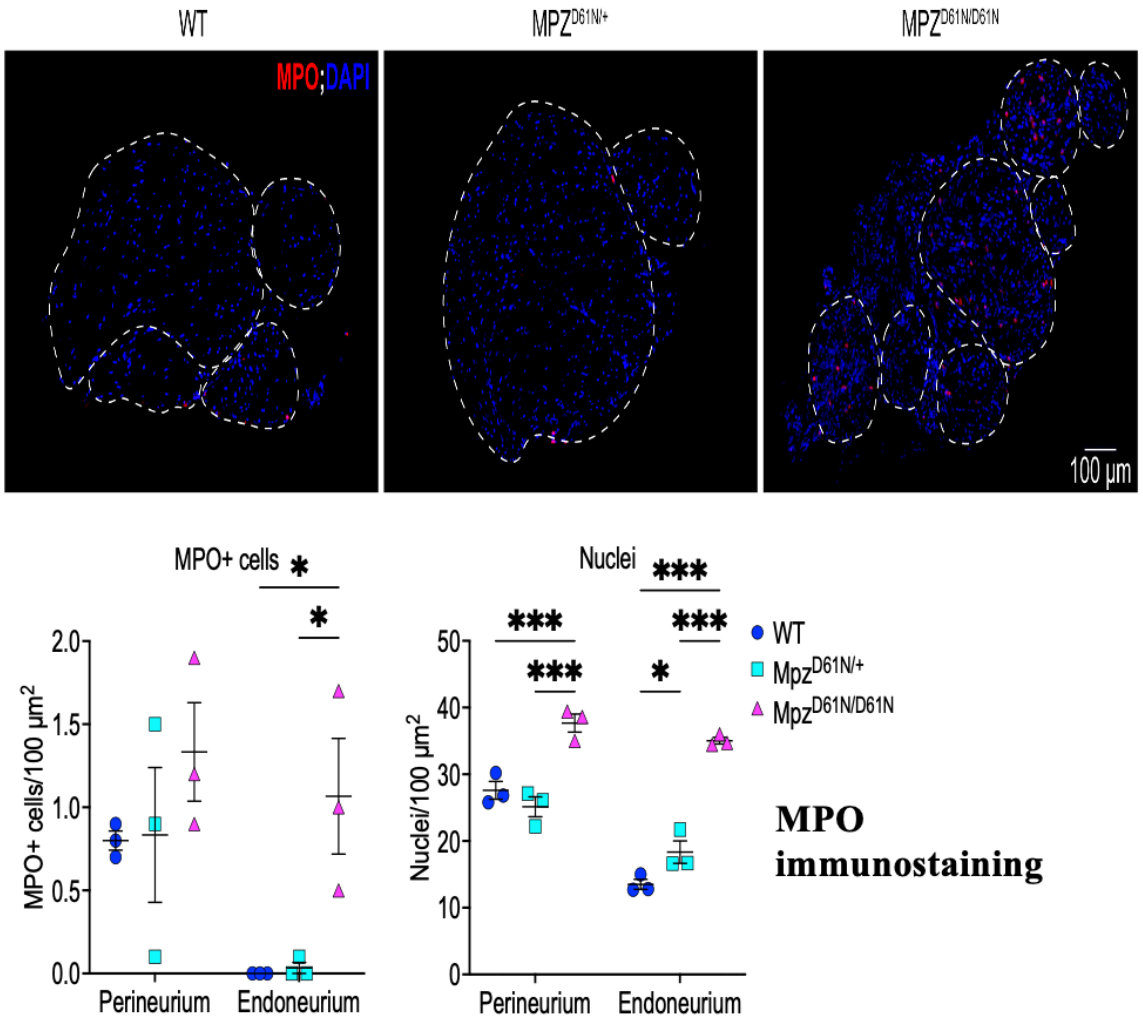

Figure 12. Immunofluorescent staining for myeloperoxidase (MPO) showing an increased density of MPO⁺ cells in the sciatic nerve of homozygous mutant mice, along with an increased nuclear density in the endoneurium of both MPZ^D61N^ heterozygous and homozygous mice.

Traumatic nerve injury (TNI) model: C57BL/6 mice

Twenty-one out of twenty-four mice with sciatic nerve crush injury completed the experimental protocol. Three animals died within the first 7 days post-injury due to hemorrhagic shock.

MRI analysis showed an increase in nerve size proximal to the lesion at 14 days compared to 7 days post-injury, associated with an elevated T2 signal. A significant reduction in T2 values was observed at 90 days compared to 14 days ($p < 0.02$). These findings are consistent with increased fluid content within the nerve due to intraneural edema. No significant difference in fractional anisotropy (FA) was observed proximal to the lesion compared to the contralateral limb.

Affected limb	**muscle T2fws (FF%)**	**nerve T1(ms)**	**nerve T2 (ms)**	**FA**	**nerve T2* (delta pre-post contrast)**
7 gg	5.3 ± 1	2035.31 ± 99	53.23 ± 2.2	0.53±0.17	-3 ± 0.34
14 gg	5.7 ± 1.2	2412.19 ± 45	**68.23 ± 3.6**	0.58±0.09	-4 ±1.2
90 gg	5.8 ± 0.7	2234.45 ±22	**59.23 ± 4.2**	0.57±0.06	-3,8 ±1.2

Table 8. Mean values ± standard deviation of MRI parameters in TNI model.

Contralateral limb	**muscle T2fws (FF%)**	**nerve T1(ms)**	**nerve T2 (ms)**	**FA**	**nerve T2* (delta pre-post contrast)**
7 gg	4.9 ± 0.8	1986.34 ± 102	51.25 ± 2.6	0.51±0.11	-3.2 ± 0.36
14 gg	5.4 ± 1.1	2400.19 ± 68	**53.12 ± 3.2**	0.54±0.09	-3.1 ± 1.2
90 gg	5.3 ± 0.4	2200.19 ± 45	**52.13 ± 3.1**	0.49±0.1	-3,8 ±1.2

Table 9. Mean values ± standard deviation of MRI parameters in healthy control (contralateral limb).

In our study, we were unable to demonstrate an increase in contrast agent uptake at the level of the nerve, despite the presence of an increase inflammatory infiltrate. This finding contrasts with previous studies in which an increase in SPION uptake in nerve and muscle tissue was observed (145). The explanation is probably related to the difference in the animal model used (mouse vs. rat), as the mouse nerve is smaller, more challenging to sample, associated with a less favorable signal-to-noise ratio.

MicroPET imaging analysis, showed tracer uptake in the muscles innervated by the sciatic nerve distal to the crush site supporting the highly expression of TSPO in activated macrophages.

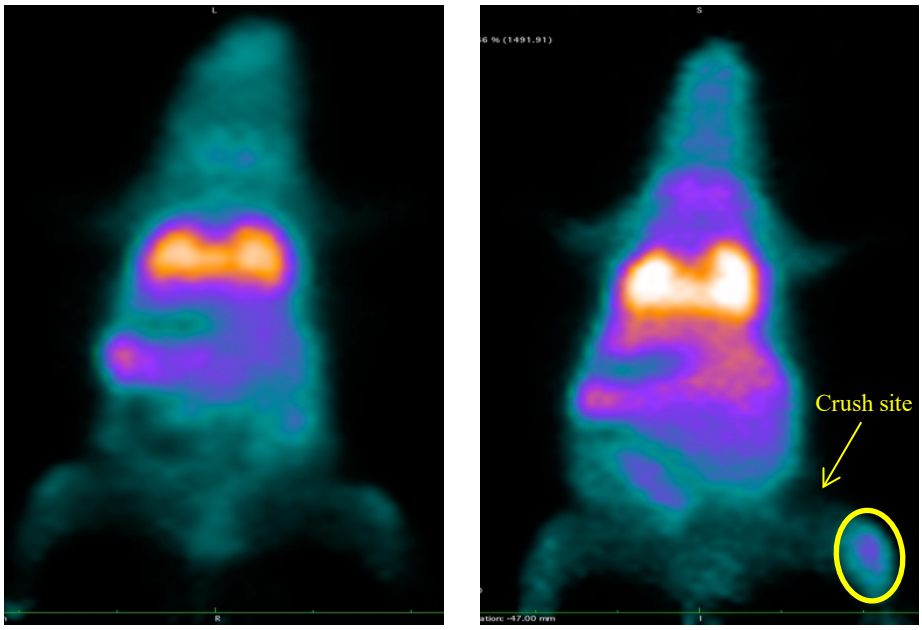

Figure 13. MicroPET images of a healthy control (left) and a mouse with traumatic nerve injury (right). On the right the yellow ellipse indicates increased uptake in the hind limb distal to the sciatic nerve crush site.

The hanging wire test showed a significant difference ($p < 0.04$) between the injured limb and the contralateral one at all time point, with a significant reduction in strengh and mobility on the affected side.

Histological analysis, at days 7 and 14, revealed a CD68+ and MPO+ inflammatory infiltrate in the muscle innervated by the injured sciatic nerve, while at day 90 the infiltrate was predominantly composed of CD11b+ macrophages. Iron-containing particles were consistently observed within macrophages and confirmed by Prussian blue staining. Despite the consistent presence of these iron particles in macrophages, contrast-enhanced MRI did not reveal signal differences between the injured limb and the contralateral one.

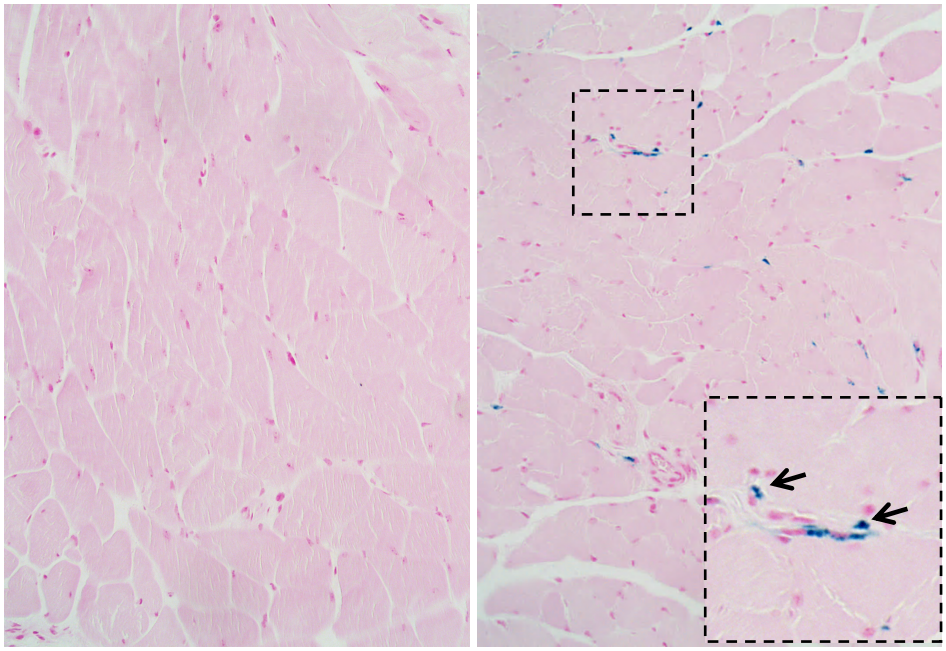

Figure 14. Unaffected limb on the left and injured limb on the right. In the denervated muscle (right), iron particles indicated by black arrows are visible, indicating the presence of macrophages that have phagocytosed the contrast agent used in MRI.

Objective 2)

The enrollment of patients with hereditary neuropathy and traumatic nerve injury has started. Although only a small number of patients has been examined so far, preliminary data are presented below.

CMT1A patients

Currently 14 patients (8 females, 6 males) have completed the observational study protocol, with a mean age of 47.57 ± 14.39 years.

MRI data were also obtained in a control group of 9 patients (5 females, 4 males), with a mean age of 46.5 ± 12.1 years.

- The inter-observer reliability of the MRI measurements was good (ICC = 0.65).
- The cross sectional area, fractional anisotropy (FA), and T1 and T2 relaxation times of the lumbosacral plexus roots and the sciatic nerve were significantly different between the two groups ($p < 0.05$)
- T1 relaxation times and FA values of L5 and S1, measured bilaterally, were significantly correlated with CMTNS ($R = 0.86$, $p = 0.013$ and $R = 0.77$, $p = 0.04$, respectively) and BBS ($R = 0.62$, $p = 0.041$ and $R = 0.75$, $p = 0.042$, respectively).
- Sciatic nerve fractional anisotropy (FA) showed significant correlations with both CMTNS ($R = 0.92$, $p = 0.010$) and BBS ($R = 0.89$, $p = 0.019$).

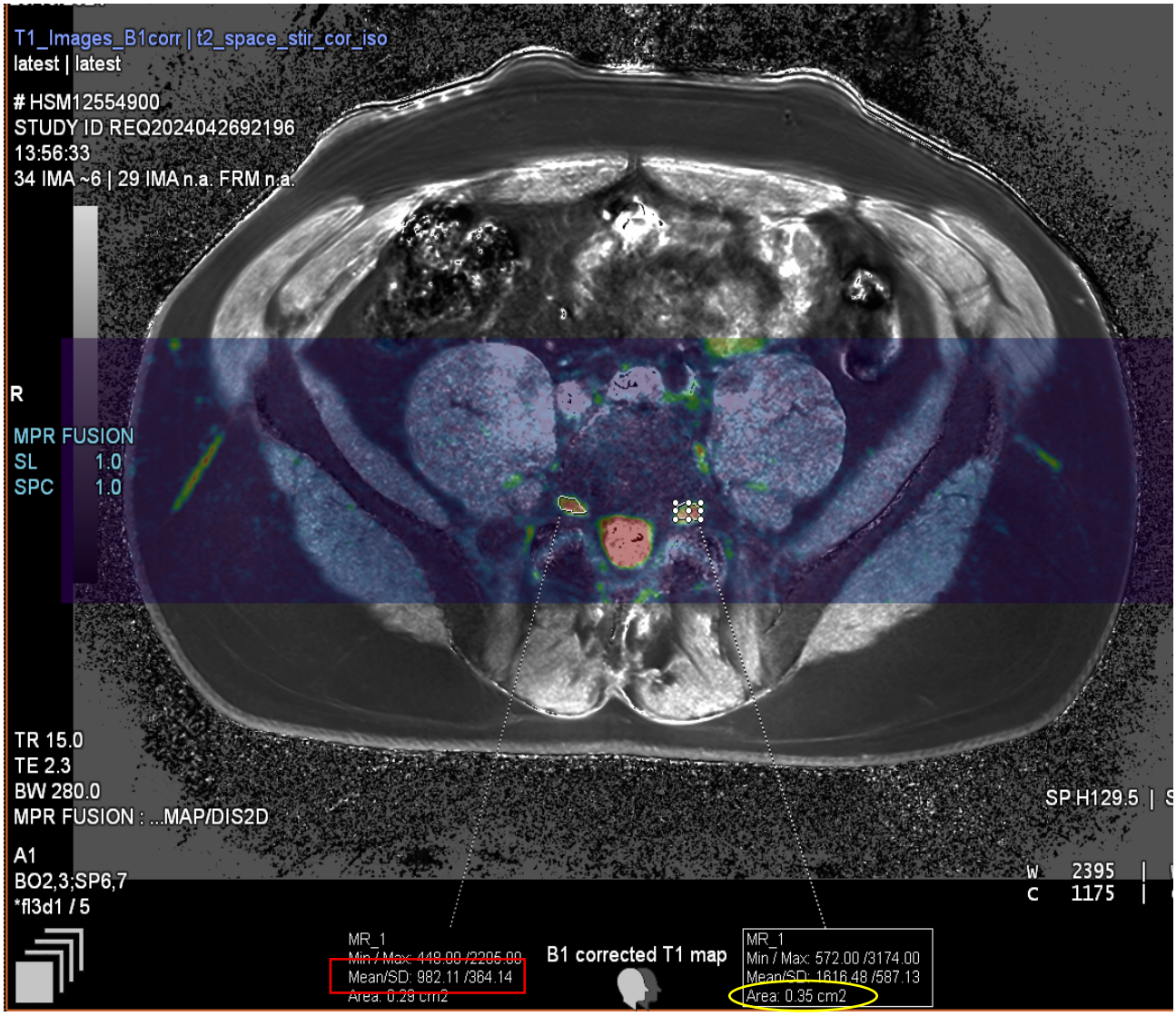

Figure 15. T1 mapping sequence in healthy control. The yellow ellipse highlights the nerve area while the red rectangle indicate the mean and standard deviation values obteined from the T1 mapping sequence.

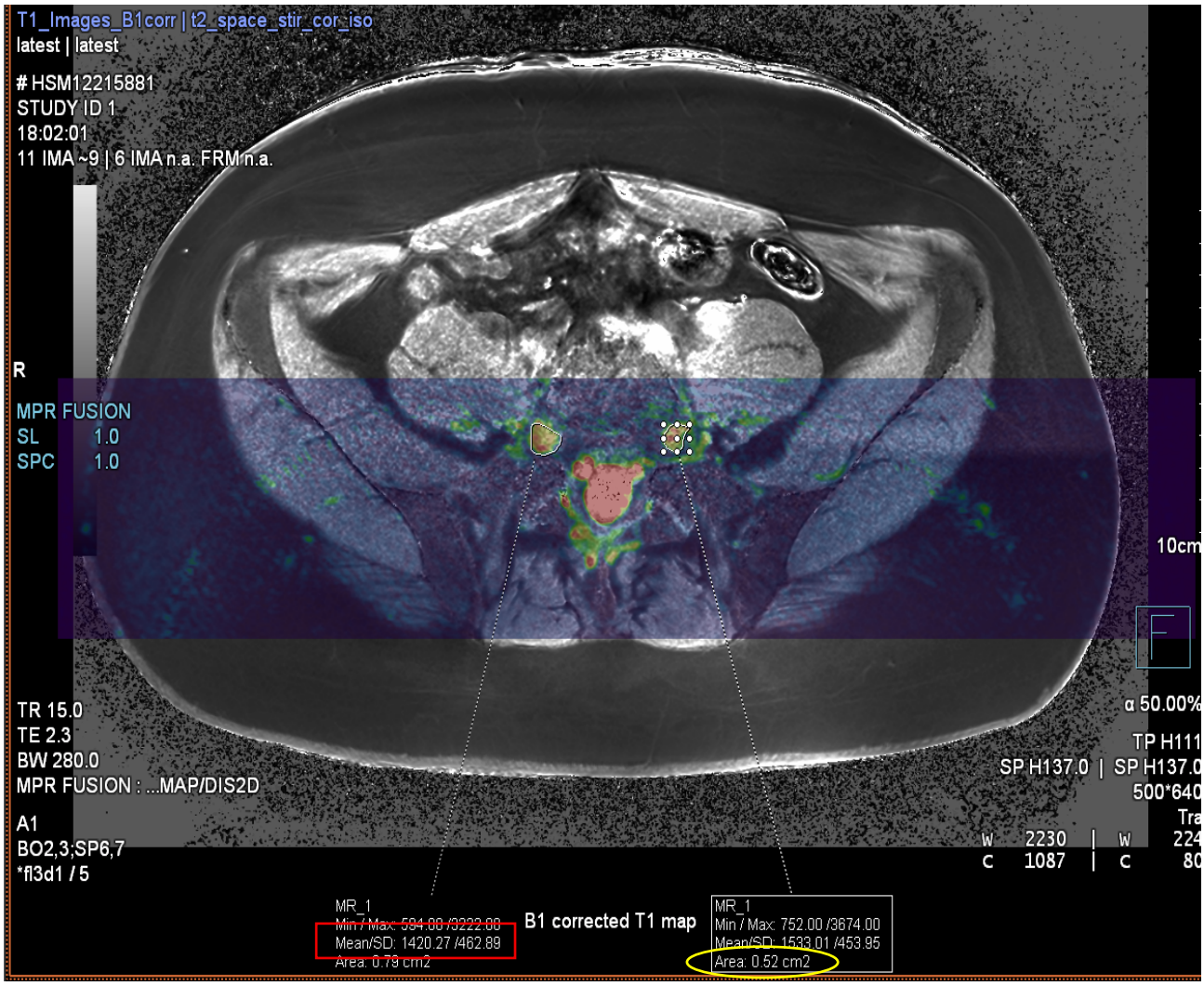

Figure 16. T1 mapping sequence in a CMT1A patient. The yellow ellipse highlights the nerve area while the red rectangle indicate the mean and standard deviation values obteined from the T1 mapping sequence.

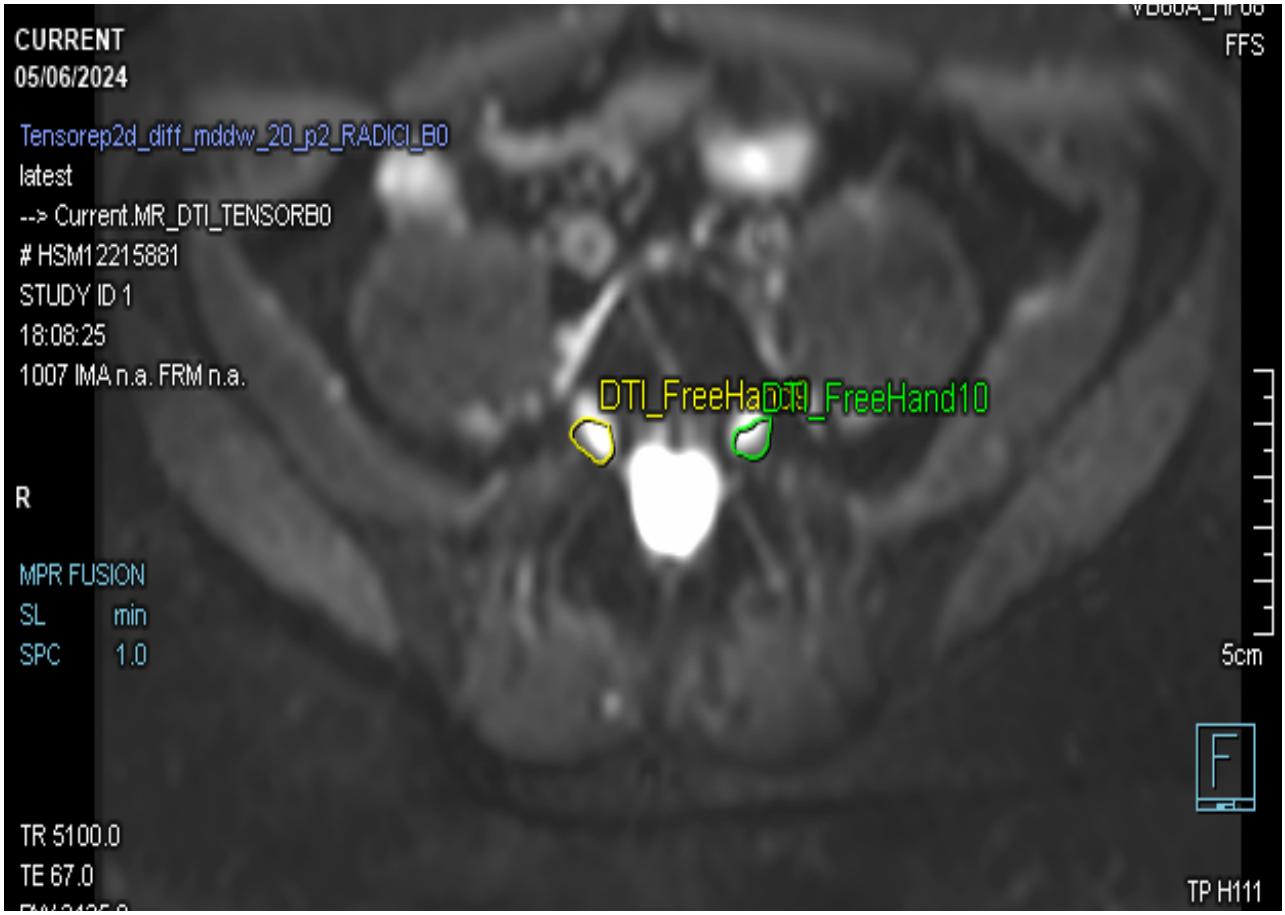

Figure 17. DTI sequence in healthy control.

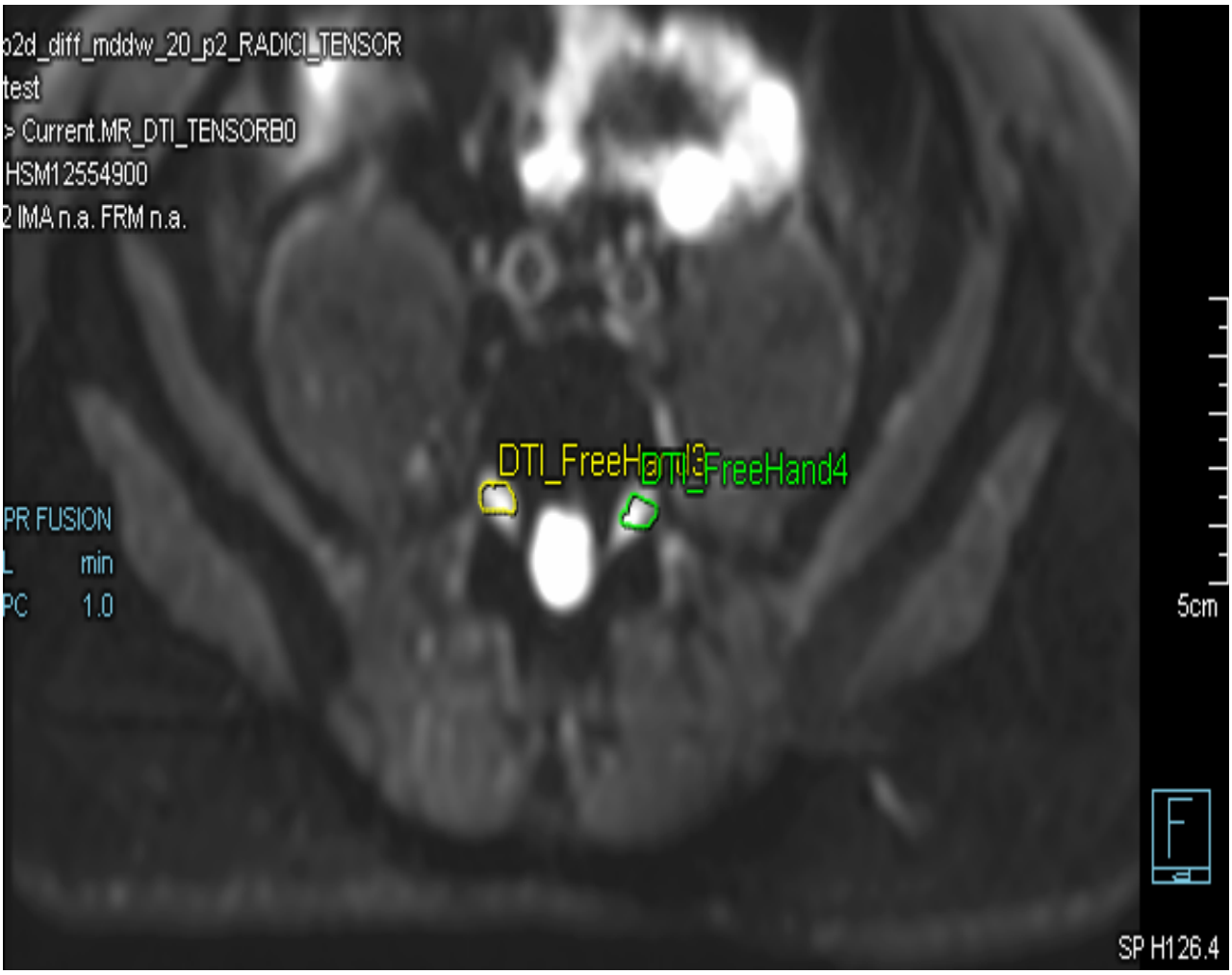

Figure 18. DTI sequence in CMT1A patient.

ID	Measurements	t2_space_stir_co...	B0	ADC	TRACEW	FA	RD	AD
DTI_FreeHand3	Mean	136.81	367.17	1366.75	93.79	257.71	1174.67	1750.63
	StdDev	36.87	80.99	87.44	23.6	43.81	98.92	104.66
	Min / Max	51 / 184	229 / 489	1268 / 1652	48 / 130	172 / 334	1073 / 1512	1580 / 1967
	(Area cm2)	0.38	0.38	0.38	0.38	0.38	0.38	0.38
DTI_FreeHand4	Mean	140.03	401	1372.73	101.32	295.32	1155.82	1806.5
	StdDev	26.88	82.89	52.63	21.46	46.94	62.84	105.71
	Min / Max	77 / 182	220 / 523	1284 / 1480	54 / 130	154 / 348	1034 / 1264	1540 / 1940
	(Area cm2)	0.36	0.36	0.36	0.36	0.36	0.36	0.36
DTI_FreeHand5	Mean	116.9	225.29	1511.41	46.88	361.88	1193.82	2146.24
	StdDev	30.47	126.17	194.01	24.24	95.34	193.36	312.99
	Min / Max	50 / 158	53 / 477	1154 / 1796	15 / 93	201 / 618	770 / 1516	1416 / 2628
	(Area cm2)	0.25	0.25	0.25	0.25	0.25	0.25	0.25
DTI_FreeHand6	Mean	103.04	252	1591.15	49.5	318.85	1303.85	2165.6
	StdDev	28.81	106.83	125.68	19.48	74.87	127.9	248.67
	Min / Max	50 / 149	74 / 416	1160 / 1703	19 / 81	126 / 406	933 / 1572	1604 / 2504
	(Area cm2)	0.32	0.32	0.32	0.32	0.32	0.32	0.32

Figure 19. DTI values in healthy control. The red ellipse highlights the fractional anisotropy (FA) value.

ID	Measurements	t2_space_stir_co...	B0	ADC	TRACEW	FA	RD	AD
DTI_FreeHand9	Mean	137.43	353.3	1381.9	89.15	288.6	1173.33	1799.2
	StdDev	20.95	161.96	238.23	44.93	94.25	241.53	291.95
	Min / Max	71 / 191	61 / 604	817 / 1899	21 / 147	187 / 590	537 / 1654	1165 / 2394
	(Area cm2)	0.59	0.59	0.59	0.59	0.59	0.59	0.59
DTI_FreeHand10	Mean	136.78	328.24	1355.79	85.79	272.58	1146.21	1775.12
	StdDev	23.76	119.41	112.93	34.04	75.55	102.83	229.83
	Min / Max	66 / 195	131 / 490	1185 / 1571	29 / 137	133 / 477	1002 / 1395	1368 / 2420
	(Area cm2)	0.49	0.49	0.49	0.49	0.49	0.49	0.49
DTI_FreeHand11	Mean	126.4	393	1509.08	86.61	245.24	1315.92	1895.45
	StdDev	22.85	147.25	154.54	35.51	68.62	154.57	203.71
	Min / Max	72 / 185	77 / 578	1137 / 1980	23 / 135	154 / 409	938 / 1764	1416 / 2411
	(Area cm2)	0.57	0.57	0.57	0.57	0.57	0.57	0.57
DTI_FreeHand12	Mean	119.68	340.88	1434.51	81.16	243.72	1252.67	1798.09
	StdDev	17.71	112.25	205.55	30.23	83.42	211.86	225.3
	Min / Max	71 / 174	40 / 477	572 / 1926	22 / 127	92 / 642	347 / 1699	1020 / 2405
	(Area cm2)	0.65	0.65	0.65	0.65	0.65	0.65	0.65

Figure 20. DTI values in CMT1A patient. The red ellipse highlights the fractional anisotropy (FA) value.

Descriptive Statistics (summary of the results in CMT1A patients)				
	Minimum	Maximum	Mean	Std. Deviation
FDFdx	38.20	80.80	57.90	13.11
FDFsx	40.20	89.80	59.02	17.41
CMTNS	7	20	13.28	5.02
BBS	45	56	52	4.24
L5 dxT1 relax time	1464.22	3462.78	2408.64	763.55
L5 dx T2 relax time	80.98	137.81	108.77	22.51
L5 dx Mean FA	204.00	361.27	292.78	50.97
L5 sxT1 relax time	1662.62	3744.59	2374.90	861.52
L5 sx T2 relax time	87.69	170.26	107.73	29.84
L5 sx Mean FA	171.38	2028.47	575.58	647.42
S1 dx T1 relax time	1928.66	3342.45	2658.38	595.63
S1 dx T2 relax tim	81.89	226.81	124.87	48.17
S1 dx Mean FA	174.27	318.38	256.10	45.175
S1 sx T1 relax time	2183.99	3431.97	2734.37	542.02
S1 sx T2 relax time	87.13	205.66	121.92	40.83
S1sx mean FA	184.96	392.85	265.23	72.24
S2 dx T1 relax time	1541.57	3143.28	2188.93	557.99
S2 dx T2 relax time	87.41	144.14	115.92	19.64
S2 dx Mean FA	147.94	341.53	270.82	73.02
S2 sx T1 relax time	1510.34	2587.73	2006.23	395.03
S2sxT2relaxtime	89.97	155.84	119.74	25.45
S2 sx Mean FA	187.40	334.87	265.86	55.71
Sciatic nerve dx T1	1068.30	2199.73	1600.46	420.43
Sciatic nerve dx T2	38.78	83.36	57.78	14.64
Sciatic nerve dx FA	294.58	364.46	323.23	28.57
Sciatic nerve sx T1	949.79	2185.47	1601.53	473.30
Sciatic nerve sx T2	48.84	87.88	67.09	13.15
Sciatic nerve sx FA	243.27	358.42	300.97	42.53
Tibial nerve dx T1	1560.11	2099.08	1815.94	209.88
Tibial nerve dx T2	54.55	98.05	75.85	16.01
Tibial nerve dx FA	249.80	378.85	296.57	50.30
Tibial nerve sx T1	1532.67	2205.27	1809.93	281.78
Tibial nerve sx T2	66.46	126.03	84.10	24.03
Tibial nerve sx FA	229.96	343.00	285.61	52.90
Common peroneal nerve dx T1	1126.67	1799.68	1537.36	294.41
Common peroneal nerve dx T2	64.00	125.93	89.56	26.13
Common peroneal nerve dx FA	266.00	295.69	285.17	11.35
Common peroneal nerve sx T1	1254.02	1792.10	1574.09	226.87
Common peroneal nerve sx T2	68.50	101.13	84.49	13.81
Common peroneal nerve sx FA	195.09	409.88	280.49	79.49
age	24	61	47.57	14.386

Patients with traumatic nerve injury

To date, 5 patients (3 males, 2 females; mean age 35.6 ± 8.9 years) have completed the interventional study protocol, including the 180-day follow-up, while 1 patient has completed follow-up up to 90 days.

Preliminary data show that lower fractional anisotropy (FA) values at 7 and 14 days were observed in patients with poorer strength recovery (assessed by MRC) at 180 days.

However, the limited number of patients enrolled does not allow for statistically significant conclusions to be made.

Electroneurographic parameters proved to be less effective than ultrasound and MRI examinations in distinguishing neuroapraxia from high-grade neurotmesis at 15 days, as 3 out of 5 patients did not have recordable CMAPs at that time.

Objective 3)

Ultrasound is a widely used imaging thecnique that offer several advantages over other medical imaging techique: it is not invasive, low-cost, and portable. Given these benefits we aimed to evaluate ultrasound as a potential tool to assess and quantify nerve and muscle damage. We measured the sciatic nerve diameter and performed textural analisys of the muscles. These imaging parameters will be correlated with levels of inflammatory mediators in muscle and nerve tissue, as well as with motor and sensory performance with the goal of identifying advanced imaging biomarkers of disease progression.

In CMT1A rats and CMT1B mice, ultrasound images showed a statistically significant increase in the cross-sectional area of the sciatic nerve compared to healthy controls. First-order textural analysis of muscle images did not reveal any statistically significant differences either among animals of different ages or in comparison with healthy controls.

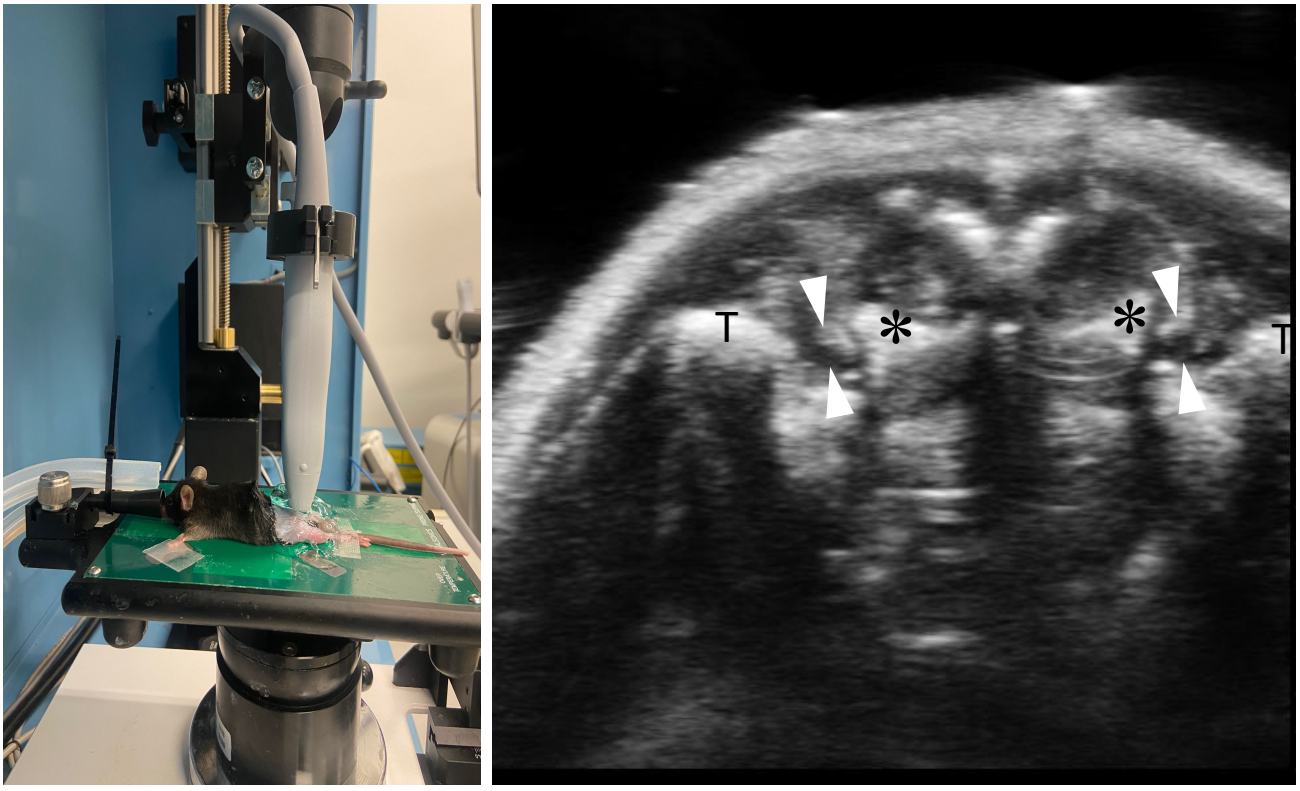

Figure 21. Ultrasound sampling technique of the sciatic nerve in mouse model. On the left the device used enables to maintain the probe in the same fixed position and helps to avoid excessive pressure on the tissue. On the right, the ultrasound image shows the sciatic nerve (arrowheads). The sciatic nerve was sampled just distal to its exit from the greater sciatic foramen (black asterisk). The greater traochanter is indicated with the letter "T".

In SOD1/G93A mice, ultrasound images showed a significant increase in muscle echo-intensity values as well as a reduction in muscle size at the advanced stage of the disease (120-day-old mice), indicating a biomarker of muscle atrophy.

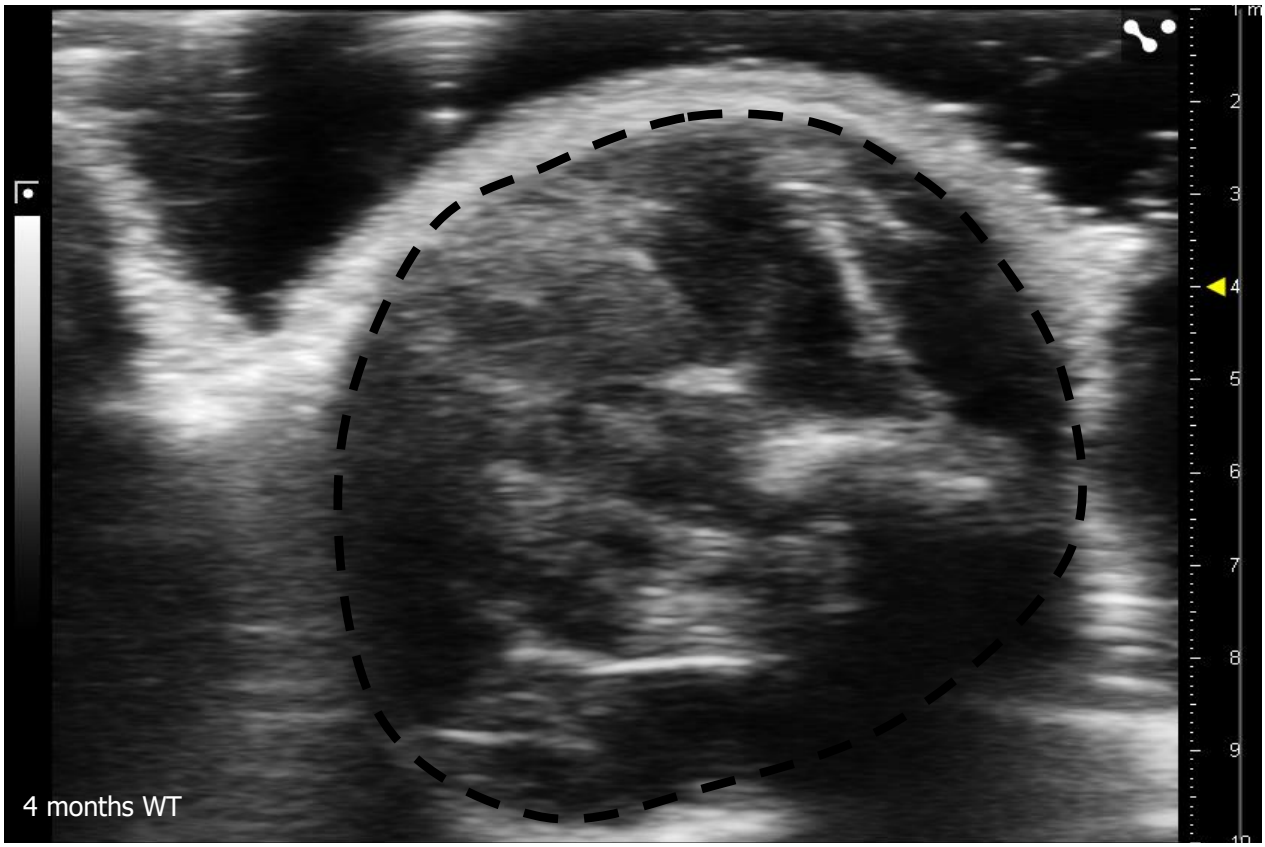

Figure 22. Axial ultrasound image of the hind limb in 4-month-old wild type mouse.

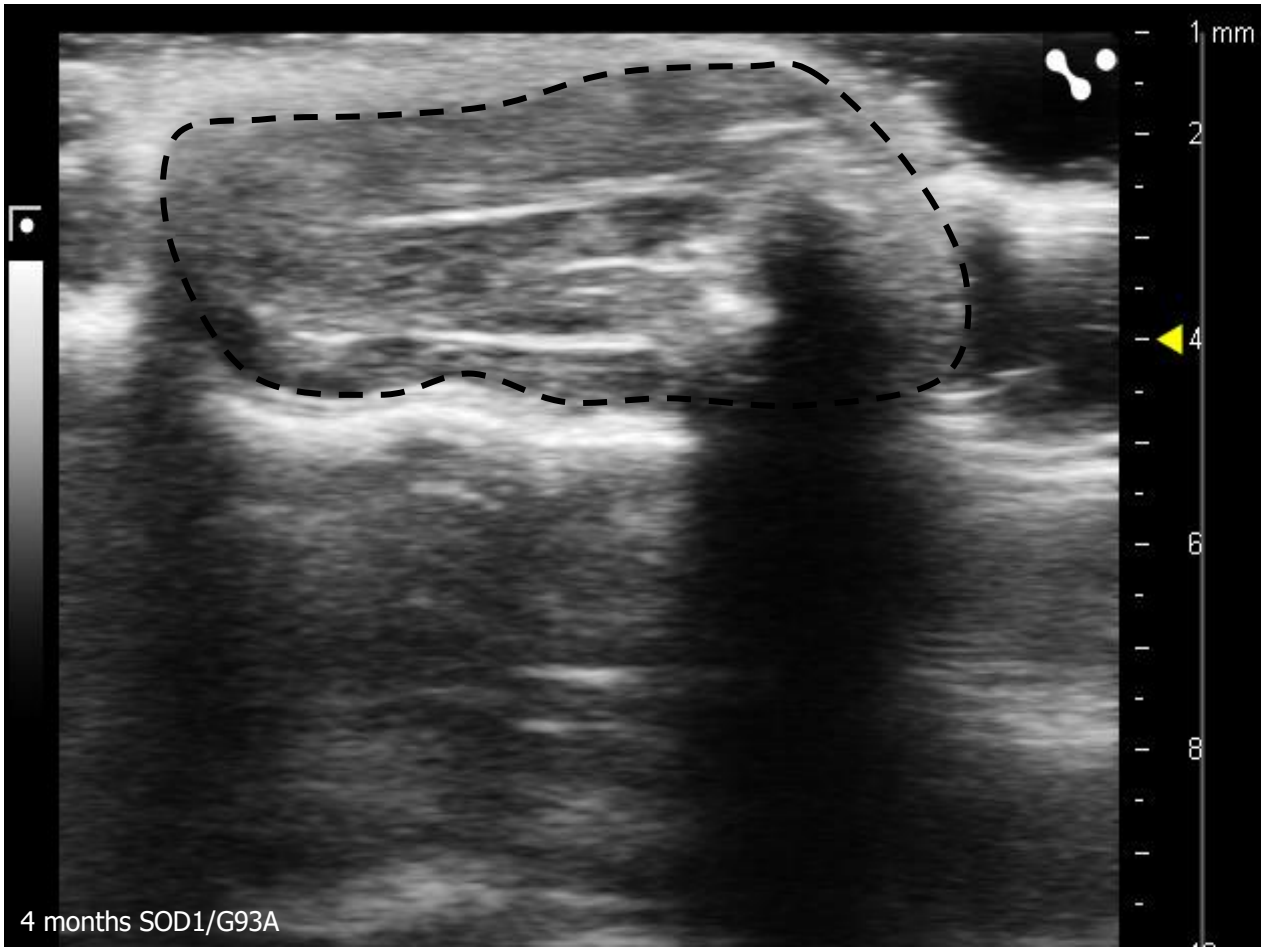

Figure 23. Axial ultrasound image of the hind limb in 4-month-old SOD1/G93A mouse which shows reduced muscle volume and increased echogenicity.

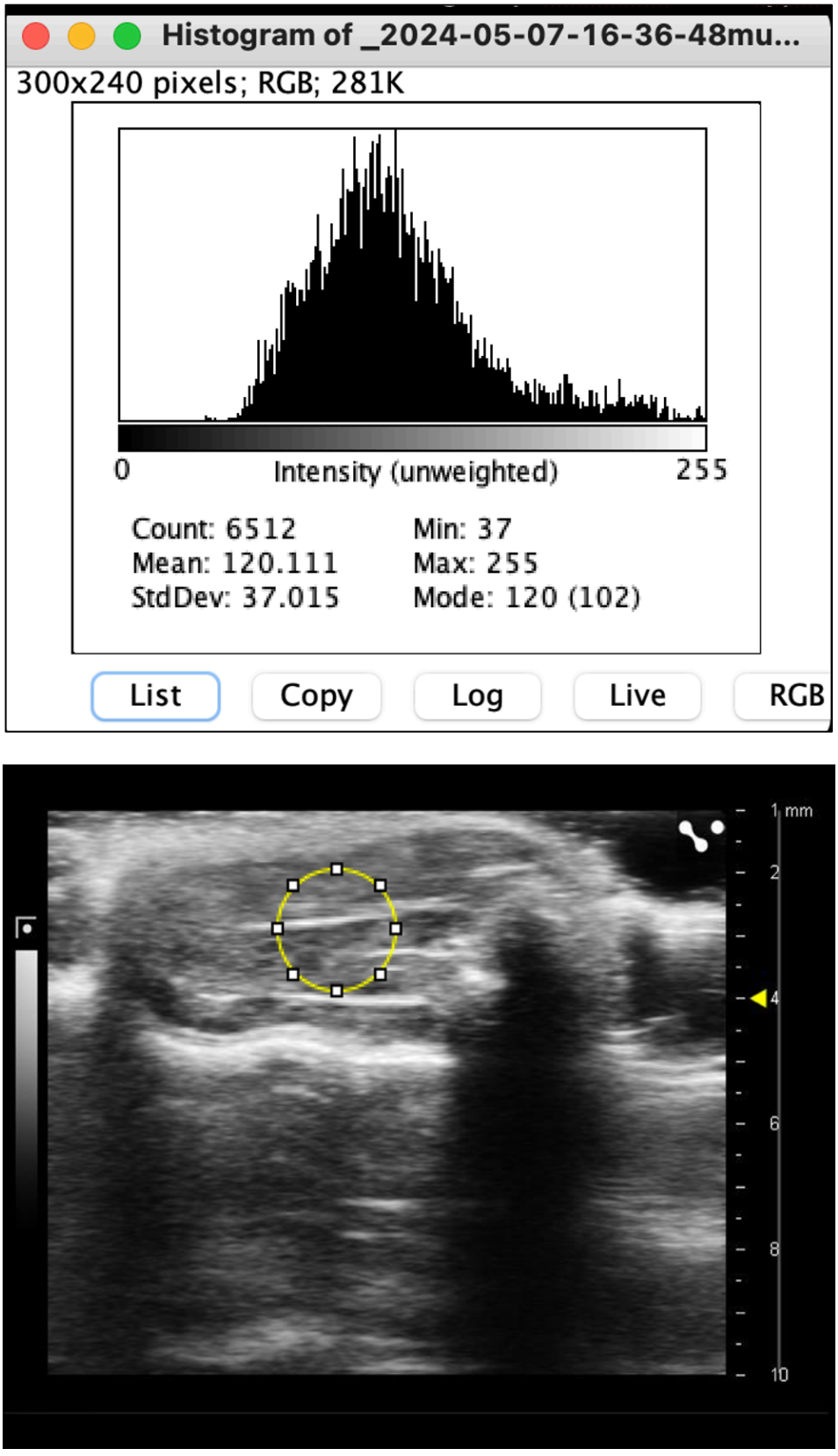

Figure 24. The images show the muscle echointensity sampling technique (a first-order texture analysis parameter) using the freewere ImageJ (NIH; Bethesda, MD,USA). The echointensity is calculated by drawing a circular ROI (yellow circle) of 150x150 pixels placed in the muscle bulk, excluding bone and subcutaneous tissue. The software provided an average gray-scale intensity value in a range from 0 to 255.

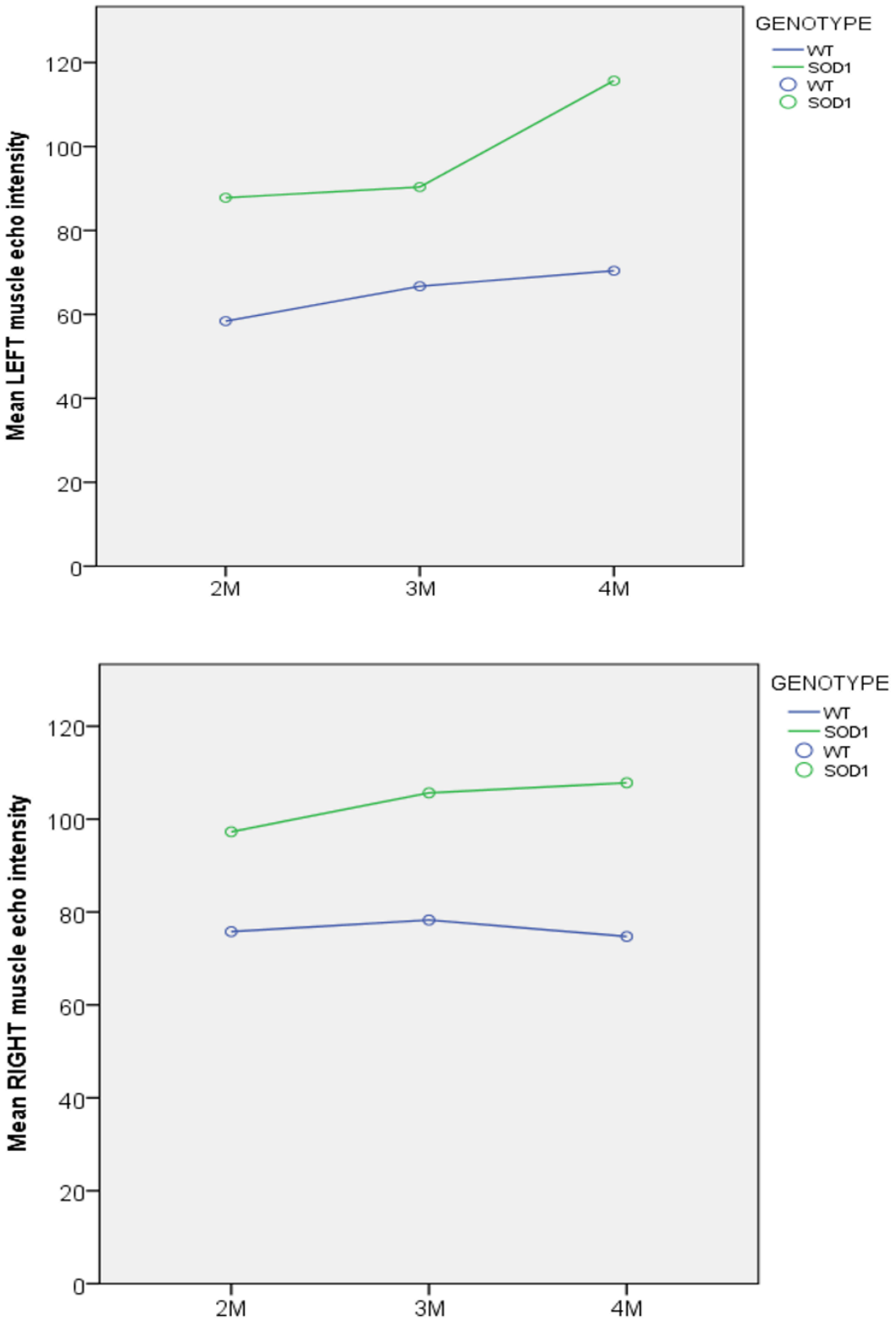

Figure 25. Muscle echointensity increases bilaterally with disease progression in SOD1/G3A mice compared to WT mice.

2M

	GENOTYPE	N	Mean	Std. Deviation	p
RIGHT muscle echo intensity	WT	3	75.77	12.24	0.1
	SOD1	3	97.27	12.79	
LEFT muscle echo intensity	WT	3	58.40	7.84	0.01
	SOD1	3	87.79	8.10	

3M

	GENOTYPE	N	Mean	Std. Deviation	p
RIGHT muscle echo intensity	WT	3	78.28	16.45	0.09
	SOD1	3	105.65	4.42	
LEFT muscle echo intensity	WT	3	66.70	18.63	0.19
	SOD1	3	90.33	18.32	

4M

	GENOTYPE	N	Mean	Std. Deviation	p
RIGHT muscle echo intensity	WT	4	74.73	18.756	0.05
	SOD1	4	107.81	19.38	
LEFT muscle echo intensity	WT	4	70.40	9.70	0.001
	SOD1	4	115.68	12.20	

Table 12. This table reports a statistically significant difference ($p<0.05$) observed in hind limbs muscle echo-intensity between 120 day-old mice and 120-day-old healthy controls, and only for the left side, between 120-day-old mice and 60-day-old mice.

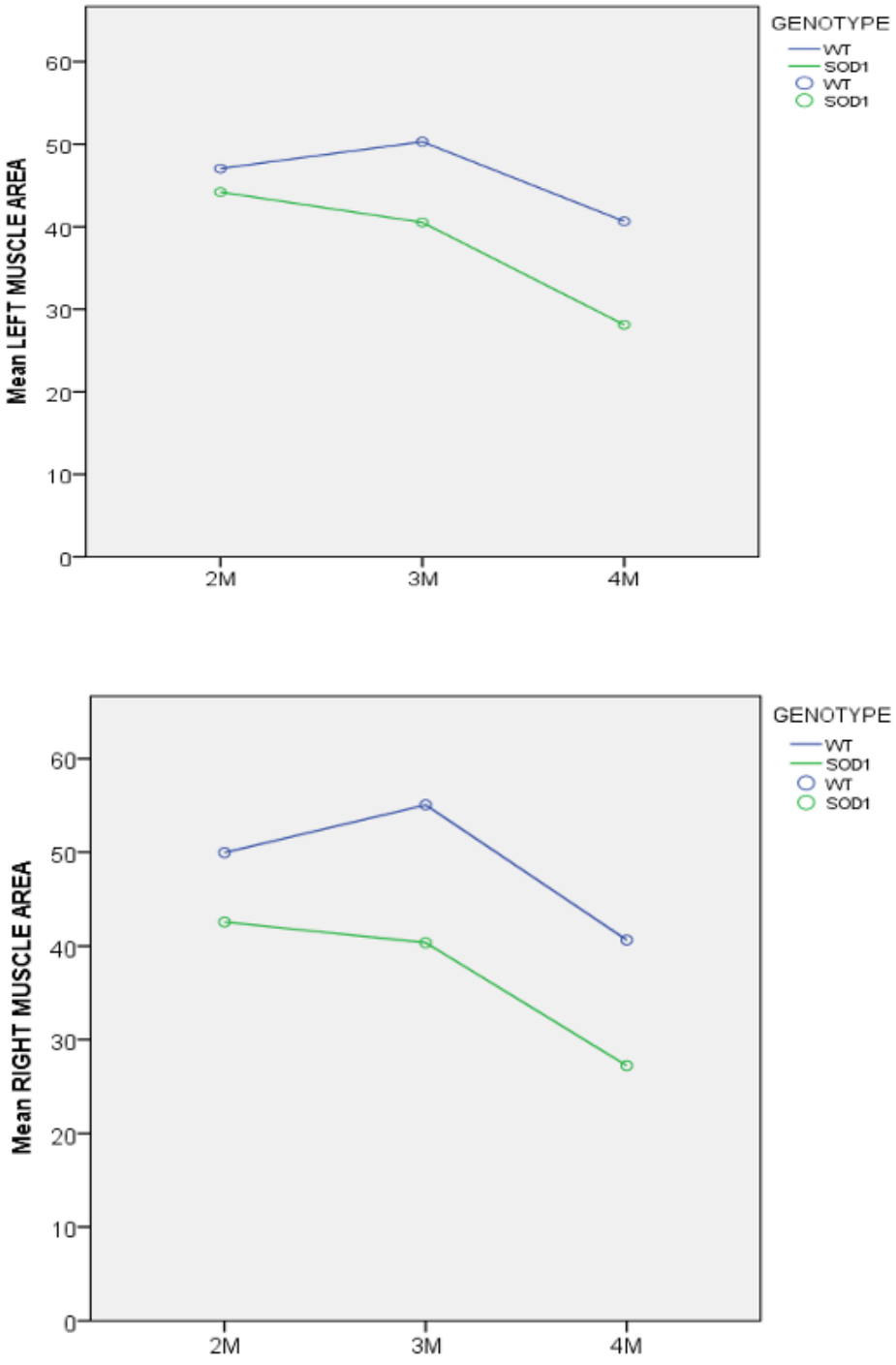

Figure 26. Muscle area decreases bilaterally with disease progression in SOD1/G3A mice compared to WT mice.

2M

	GENOTYPE	N	Mean	Std. Deviation	p
RIGHT MUSCLE AREA	WT	3	49.97	4.34	0.14
	SOD1	3	42.55	5.67	
LEFT MUSCLE AREA	WT	3	47.04	0.791	0.20
	SOD1	3	44.20	3.186	

3M

	GENOTYPE	N	Mean	Std. Deviation	p
RIGHT MUSCLE AREA	WT	3	55.05	12.05	0.14
	SOD1	3	40.35	6.92	
LEFT MUSCLE AREA	WT	3	50.30	10.73	0.22
	SOD1	3	40.53	4.60	

4M

	GENOTYPE	N	Mean	Std. Deviation	p
RIGHT MUSCLE AREA	WT	4	40.64	6.35	0.022
	SOD1	4	27.23	6.00	
LEFT MUSCLE AREA	WT	4	40.66	5.26	0.019
	SOD1	4	28.13	5.80	

Table 13. This table reports a statistically significant difference ($p<0.05$) observed in muscles area of the hind limbs in 120-day-old mice compared to 120-day-old healthy controls.

Discussion

In this study, we compared three distinct models of peripheral nerve denervation:

(1) Genetically inherited peripheral neuropathy (Charcot-Marie-Tooth disease)

(2) Amyotrophic lateral sclerosis (ALS)

(3) Traumatic nerve injury

Our primary aim was to evaluate the extent and nature of immune system activation across these models, and to explore its potential role in both nerve degeneration and regeneration.

We observed clear differences in immune activation among the three models.

Charcot-Marie-Tooth (CMT) disease constitutes the most common form of inherited peripheral neuropathy (8). The most frequently implicated genes in Charcot-Marie-Tooth (CMT) disease are three myelin-related genes: PMP22, P0, and Cx32. The most common demyelinating subtype, CMT1A, is caused by a 1.5-Mb genomic duplication on chromosome 17 that includes the peripheral myelin protein 22 gene (PMP22). This gene duplication leads to PMP22 overexpression, which in turn results in peripheral nervous system (PNS) demyelination, as evidenced by reduced nerve conduction velocities and segmental demyelination observed in nerve biopses (10).

Less commonly, CMT1 is caused by point mutations in the PMP22 gene or in the gene encoding myelin protein zero (MPZ), the latter associated with the CMT1B subtype (11,13,146).

In the literature, several studies have suggested that neuroinflammation, specifically lymphocytic and macrophage infiltration, has been observed in both CMT1A and CMT1B, supporting the hypothesis that these immune responses may contribute to the degenerative features and progression of the disease (10,147). Furthermore, studies in the literature, on an homozygous mouse model of CMT1B, have shown that endogenous antibodies contribute to early macrophage-driven demyelination and accelerate the disease progression. These findings support the notion that the innate and adaptive immune systems are intricately linked in this genetic context (148). The underlying mutation may play a pivotal role by inducing structural disruptions in myelin, potentially unmasking normally

sequestered neural antigens. This antigen exposure could, in turn, initiate a secondary autoimmune response, adding an immune-mediated component to the pathogenesis of peripheral nerve damage

In our study, no evidence of immune system involvement was observed in the CMT1A model, indicating an absence of neuroinflammatory activity in this chronic genetic neuropathy. On the other hand, in the homozygous CMT1B model, which does not have a direct human correlate, we observed a clear macrophage infiltrate within the peripheral nerve. However, the functional significance of this inflammatory response remains uncertain. This supports the hypothesis that inflammatory infiltration may not be a common feature across all peripheral neuropathies, but rather a phenomenon limited to specific subtypes. In any case, further studies are necessary to determine whether this inflammatory response plays a pathogenic role in exacerbating the disease phenotype or merely represents a secondary epiphenomenon.

Regarding the application of MRI in CMT1A disease, to date there are few studies in the literature that have evaluated the application of T1 mapping in the peripheral nervous system making it a potentially novel approach. Until now, T1 mapping has been primarily utilized in cardiac imaging to quantify intrinsic pathological processes affecting the myocardium, including diseases involving the intracellular or extracellular compartements such as edema, amyloidosis and iron overload with particular focus on myocardial fibrosis; it also provide information about myocardial inflammation, infiltrative diseases and storage disorders (127).

Generally, in pathological conditions, such as CMT1a disease, an increased water content within the nerve may occur, representing a potential confounding factor in nerve imaging as it can affect the T1 signal. This aspect remain to be fully clarified. Notably, we observed a statistically significant correlations with T1 mapping, but not with T2 mapping, which indicate that T1 provides distinct information. If the changes were solely due to water content, one would expect concordant results between T1 and T2 mapping. Instead, T1 mapping correlated more strongly with DTI parameters. This suggests that although T1 may be influenced by water, it also detects additional pathological features within the nerve, likely related to fibrosis.

With regard to humans, the most promising findings that emerged was the potential use of T1 mapping in MRI as a biomarker of disease severity in certain types of peripheral neuropathy, especially in CMT1a patients. The exact histological alteration underlying the T1 signal change remains unclear, although intraneural fibrosis and increased collagen content are possible candidates. Nevertheless, this finding clearly merits further investigation to validate its relevance.

To date, the immune response model most thoroughly characterized among the various forms of denervation is the one associated with traumatic nerve injury. In this context, macrophages play a pivotal role in modulating the inflammatory response and supporting nerve repair processes. Following peripheral nerve transection, the distal segment rapidly undergoes Wallerian degeneration. During this phase, endoneurial macrophages express CCL7 ligands, which promote the recruitment and activation of both classically activated (M1) and alternatively activated (M2) macrophages at the lesion site (3,4). The temporal dynamics and distinct cytokine expression profiles of M1 and M2 macrophages indicate that these subsets may exert complementary and stage-specific functions during nerve repair following injury (6). In the early post-injury phase, within approximately three days, perisynaptic Schwann cells (pSCs) located around denervated synapses actively recruit macrophages to clear debris from degenerating axons and myelin sheaths. This macrophage-mediated clearance is a critical step in creating a permissive microenvironment for regeneration. Macrophage density typically peaks around one week after injury, and in concert with the activity of pSCs, these immune cells contribute to the reinnervation process by promoting angiogenesis, axonal sprouting, and overall tissue remodeling. Current evidence suggests that macrophages may play a comparable role at the neuromuscular junction (NMJ). However, the specific macrophage phenotypes active at this site and their precise functional contribution to the reinnervation process have yet to be fully elucidated (7). In traumatic nerve injury model our study confirmed what is already well-documented in the literature: the immune system actively participates in the repair process. In this context, immune cell recruitment, particularly macrophages, plays a beneficial role by clearing debris and supporting axonal regeneration. In our study, MRI images were unable to demonstrate an increase in

macrophage-specific contrast agent uptake at the level of the nerve, despite the presence of an increase inflammatory infiltrate. This finding contrasts with previous studies in which an increase in SPION uptake in nerve and muscle tissue was observed (145). The explanation is probably related to the difference in the animal model used (mouse vs. rat), as the mouse nerve is smaller, more challenging to sample, associated with a less favorable signal-to-noise ratio. Moreover, the use of functional MRI sequences was limited by several technical challenges, including the sub-millimeter diameter of the murine peripheral nerve and the high noise levels associated with 7 Tesla MRI scanners, which reduced the reproducibility and reliability of the acquired data.

In the context of traumatic nerve injury, the existing literature on the role of MRI and ultrasound is limited and lacks a systematic approach. Specifically, previous studies have not evaluated nerve damage at well defined timepoints and did not incorporate quantitative MRI sequences into their imaging protocols. Our study addresses this gap by employing a structured methodology and advanced imaging techniques.

Similarly, ultrasound imaging of the murine muscle was only effective in detecting pathological changes at advanced stages of disease, when severe muscle atrophy had already occurred. As such, ultrasound appears less suitable for early-stage monitoring in preclinical models of neuropathy.

As expected, among the imaging techniques, microPET proved to be the most sensitive in detecting alterations associated with immune system activation. In our study it was able to clearly identify inflammatory infiltrates in the traumatic nerve injury model, and also to detect early metabolic alterations in SOD1/G93A transgenic mice.

Amyotrophic lateral sclerosis (ALS), is a neurodegenerative disorder characterized by the progressive loss of both upper and lower motor neurons. Traditionally, ALS has been conceptualized primarily as a disease of the motor neurons themselves, with skeletal muscle alterations regarded merely as secondary consequences of motor neuron loss, axonal degeneration, and neuromuscular junction disruption. However, increasing evidence has challenged this neuron-centric view, demonstrating that motor neurons, skeletal muscle fibers, and Schwann cells should be viewed as functionally

interdependent components of a single neuromuscular unit, rather than as separate or isolated elements. This evolving perspective suggests that skeletal muscle cells may play a more active role in ALS pathogenesis, shifting their status from passive targets of neuronal degeneration to potential contributors to the disease process (149). Our experimental data are consistent with this hypothesis and support the occurrence of a selective, cell-autonomous degeneration within the skeletal muscle. This feature is reflected by both the upregulation of TSPO expression and the increased uptake of its specific radioligand, [^{18}F]DPA-714. Although the present data do not conclusively demonstrate that binding to TSPO is the mechanism responsible for the enhanced tracer uptake, our results show that the skeletal muscle of SOD1^G93A mice exhibits a significant accumulation of radioactivity after [^{18}F]DPA-714 administration, as revealed by microPET imaging. This observation was consistent with TSPO expression as confirmed by immunohistochemistry and Western blot analyses. Tracer uptake was specifically localized to myocytes, with no evidence of significant inflammatory infiltrates detected by hematoxylin/eosin staining or CD68 immunohistochemistry. In contrast it demonstrated progressive myofiber atrophy in the transgenic mice compared to controls; the nuclei in the mutated skeletal muscle appeared more numerous, enlarged, and positioned closer together, likely as a consequence of tissue degeneration. These findings suggest that [^{18}F]DPA-714 is not an exclusive marker of inflammation but may also reflect a direct reaction of damaged tissue (150). Moreover, these changes appear to be more closely related to muscle metabolic dysfunction rather than to direct neuroinflammation.

Interestingly, our study revealed clear differences in immune activation across the three models. In the case of traumatic nerve injury, both microPET imaging and Prussian blue staining detected inflammatory infiltrates in the muscles innervated by the sciatic nerve in the mouse model. In contrast, no significant immune activation was observed at the muscle level in the other models. These findings suggest that muscle atrophy due to denervation may be indirectly influenced by the immune system, although there is no evident accumulation of intramuscular macrophages.

We are now currently working to establish correlations between advanced imaging metrics, both from nerve and muscle, and the extent of inflammatory cell infiltration, with the goal of identifying non-invasive biomarkers of disease activity.

References

1. Bongers KS, Fox DK, Ebert SM, Kunkel SD, Dyle MC, Bullard SA, et al. Skeletal muscle denervation causes skeletal muscle atrophy through a pathway that involves both Gadd45a and HDAC4. Am J Physiol Endocrinol Metab. 2013 Oct 1;305(7).
2. Rios R, Jablonka-Shariff A, Broberg C, Snyder-Warwick AK. Macrophage roles in peripheral nervous system injury and pathology: Allies in neuromuscular junction recovery. Vol. 111, Molecular and Cellular Neuroscience. Academic Press Inc.; 2021.
3. Tomlinson JE, Žygelyte E, Grenier JK, Edwards MG, Cheetham J. Temporal changes in macrophage phenotype after peripheral nerve injury. J Neuroinflammation. 2018 Jun 15;15(1).
4. Bombeiro AL, Pereira BTN, de Oliveira ALR. Granulocyte-macrophage colony-stimulating factor improves mouse peripheral nerve regeneration following sciatic nerve crush. European Journal of Neuroscience. 2018 Sep 1;48(5):2152–64.
5. Gaudet AD, Popovich PG, Ramer MS. Wallerian degeneration: Gaining perspective on inflammatory events after peripheral nerve injury. Vol. 8, Journal of Neuroinflammation. 2011.
6. Zigmond RE, Echevarria FD. Macrophage biology in the peripheral nervous system after injury. Vol. 173, Progress in Neurobiology. Elsevier Ltd; 2019. p. 102–21.
7. Ydens E, Amann L, Asselbergh B, Scott CL, Martens L, Sichien D, et al. Profiling peripheral nerve macrophages reveals two macrophage subsets with distinct localization, transcriptome and response to injury. Nat Neurosci. 2020 May 1;23(5):676–89.
8. Vance JM. Hereditary motor and sensory neuropathies. Vol. 28, JMed Genet. 1991.
9. Skre H. Genetic and clinical aspects of Charcot-M a rie-Tooth's disease.
10. Kobsar I, Hasenpusch-Theil K, Wessig C, Müller HW, Martini R. Evidence for macrophage-mediated myelin disruption in an animal model for Charcot-Marie-Tooth neuropathy type 1A. J Neurosci Res. 2005 Sep 15;81(6):857–64.

11. Pareyson D, Marchesi C. Diagnosis, natural history, and management of Charcot-Marie-Tooth disease. Vol. 8, The Lancet Neurology. 2009. p. 654–67.

12. Lupski JR, Montes De Oca-Luna R, Slaugenhaupt S, Pentao L, Guzzetta V, Trask BJ, et al. DNA Duplication Associated with Charcot-Marie-Tooth Disease Type 1 A. Vol. 66, Cell. 1991.

13. DUPLICATION IN CHROMOSOME 17p11.2 IN CHARCOT-MARIETOOTH NEUROPATHY TYPE la (CMT la).

14. Barisic N, Claeys KG, Sirotković-skerlev M, Löfgren A, Nelis E, De Jonghe P, et al. Charcot-Marie-Yooth disease: A clinico-genetic confrontation. Vol. 72, Annals of Human Genetics. 2008. p. 416–41.

15. Szigeti K, Lupski JR. Charcot-Marie-Tooth disease. European Journal of Human Genetics. 2009;17(6):703–10.

16. Pareyson D. Axonal Charcot-Marie-Tooth disease: The fog is only slowly lifting. Vol. 68, Neurology. Lippincott Williams and Wilkins; 2007. p. 1649–50.

17. Dubourg O, Tardieu S, Birouk N, Gouider R, Le Âger JM, Maisonobe T, et al. The frequency of 17p11.2 duplication and Connexin 32 mutations in 282 Charcot-Marie-Tooth families in relation to the mode of inheritance and motor nerve conduction velocity [Internet]. Available from: www.elsevier.com/locate/nmd

18. Boerkoel CF, Takashima H, Garcia CA, Olney RK, Johnson J, Berry K, et al. Charcot-Marie-Tooth disease and related neuropathies: Mutation distribution and genotype-phenotype correlation. Ann Neurol. 2002;51(2):190–201.

19. Szigeti K, Garcia CA, Lupski JR. Charcot-Marie-Tooth disease and related hereditary polyneuropathies: Molecular diagnostics determine aspects of medical management. Genetics in Medicine. 2006 Feb;8(2):86–92.

20. Verhoeven K, Claeys KG, Züchner S, Schröder JM, Weis J, Ceuterick C, et al. MFN2 mutation distribution and genotype/phenotype correlation in Charcot-Marie-Tooth type 2. Brain. 2006;129(8):2093–102.

21. Vallat JM, Tazir M, Magdelaine C, Sturtz F, Grid D. Autosomal-Recessive Charcot-Marie-Tooth Diseases [Internet]. Vol. 64, J Neuropathol Exp Neurol. 2005. Available from: https://academic.oup.com/jnen/article-abstract/64/5/363/2916597

22. Ouvrier R, Geevasingha N, Ryan MM. Autosomal-recessive and X-linked forms of hereditary motor and sensory neuropathy in childhood. Vol. 36, Muscle and Nerve. 2007. p. 131–43.

23. Pareyson D, Scaioli V, Laurà M. Clinical and electrophysiological aspects of charcot-marie-tooth disease. Vol. 8, NeuroMolecular Medicine. Humana Press Inc.; 2006. p. 3–22.

24. Krajewski KM, Lewis RA, Fuerst DR, Turansky C, Hinderer SR, Garbern J, et al. Neurological dysfunction and axonal degeneration in Charcot-Marie-Tooth disease type 1A. Vol. 123, Brain. 2000.

25. Scherer SS, Wrabetz L. Molecular mechanisms of inherited demyelinating neuropathies. Glia. 2008;56(14):1578–89.

26. Shy ME, Lupski JR, Chance PF, Klein CJ, Dyck PJ. Hereditary Motor and Sensory Neuropathies: An Overview of Clinical, Genetic, Electrophysiologic, and Pathologic Features. In: Peripheral Neuropathy: 2-Volume Set with Expert Consult Basic. Elsevier; 2005. p. 1623–58.

27. Harding AE, Thomas PK. THE CLINICAL FEATURES OF HEREDITARY MOTOR AND SENSORY NEUROPATHY TYPES I AND II. Vol. 103, Brain. 1980.

28. Lupski JR, Garcia CA. Molecular Genetics and Neuropathology of Charcot-Marie-Tooth Disease Type 1A. In: Brain Pathology. 1992. p. 337–49.

29. Hoogendijk JE, de Visser M, Bolhuis PA, Hart AAM, de Visser BWO. Hereditary motor and sensory neuropathy type I: Clinical and neurographical features of the 17p duplication subtype. Muscle Nerve. 1994;17(1):85–90.

30. Birouk N, Gouider R, Le Guern E, Gugenheim M, Tardieu S, Maisonobe T, et al. Charcot-Marie-Tooth disease type 1A with 17p11.2 duplication Clinical and electrophysiological phenotype study and factors influencing disease severity in 119 cases. Vol. 120, Brain. 1997.

31. Thomas PK, Marques W, Davis MB, Sweeney MG, King RHM, Bradley JL, et al. The phenotypic manifestations of chromosome 17p11.2 duplication. Vol. 120. 1997.

32. Verhamme C, Van Schaik IN, Koelman JHTM, De Haan RJ, Vermeulen M, De Visser M. Clinical disease severity and axonal dysfunction in hereditary motor and sensory neuropathy Ia. J Neurol. 2004 Dec;251(12):1491–7.

33. Garcia A, Combarros O, Calleja J, Berciano J. Charcot-Marie-Tooth disease type 1A with 17p duplication in infancy and early childhood A longitudinal clinical and electrophysiologic study. 1061.

34. Berciano J, García A, Combarros O. Initial semeiology in children with Charcot-Marie-Tooth disease 1A duplication. Muscle Nerve. 2003 Jan 1;27(1):34–9.

35. Padua L, Pareyson D, Aprile I, Cavallaro T, Quattrone A, Rizzuto N, et al. Natural history of CMT1A including QoL: A 2-year prospective study. Neuromuscular Disorders. 2008 Mar;18(3):199–203.

36. Videler AJ, Van Dijk PJP, Beelen BA, De Visser M, Nollet F, Van Schaik IN. Motor axon loss is associated with hand dysfunction in Charcot-Marie-Tooth disease 1a [Internet]. 2008. Available from: www.neurology.org

37. Shy ME, Chen L, Swan ER, Taube R, Krajewski KM, Herrmann D, et al. Neuropathy progression in Charcot-Marie-Tooth disease type 1A. Neurology. 2008;70(5):378–83.

38. Pareyson D, Scaioli V, Laurà M. Clinical and electrophysiological aspects of charcot-marie-tooth disease. Vol. 8, NeuroMolecular Medicine. Humana Press Inc.; 2006. p. 3–22.

39. Jani-Acsadi A, Krajewski K, Shy ME. Charcot-Marie-Tooth neuropathies: Diagnosis and management. Vol. 28, Seminars in Neurology. 2008. p. 185–94.

40. Diagnostic criteria-terminology and definitions.

41. Pareyson D. Diagnosis of hereditary neuropathies in adult patients. Vol. 250, Journal of Neurology. 2003. p. 148–60.

42. Pareyson D. Differential diagnosis of Charcot-Marie-Tooth disease and related neuropathies. Vol. 25, Neurological Sciences. Springer Milan; 2004. p. 72–82.

43. Martinoli C, Schenone A, Bianchi S, Mandich P, Caponetto C, Abbruzzese M, et al. Sonography of the Median Nerve in Charcot-Marie-Tooth Disease [Internet]. 2002. Available from: www.ajronline.org

44. Gallardo E, García A, Combarros O, Berciano J. Charcot-Marie-Tooth disease type 1A duplication: Spectrum of clinical and magnetic resonance imaging features in leg and foot muscles. Brain. 2006 Feb;129(2):426–37.

45. Chung KW, Suh BC, Shy ME, Cho SY, Yoo JH, Park SW, et al. Different clinical and magnetic resonance imaging features between Charcot-Marie-Tooth disease type 1A and 2A. Neuromuscular Disorders. 2008 Aug;18(8):610–8.

46. Moloney EB, de Winter F, Verhaagen J. ALS as a distal axonopathy: Molecular mechanisms affecting neuromuscular junction stability in the presymptomatic stages of the disease. Front Neurosci. 2014;(8 JUL).

47. Kanai K, Kuwabara S, Misawa S, Tamura N, Ogawara K, Nakata M, et al. Altered axonal excitability properties in amyotrophic lateral sclerosis: Impaired potassium channel function related to disease stage. Brain. 2006;129(4):953–62.

48. De Carvalho M, Swash M. Fasciculation potentials and earliest changes in motor unit physiology in ALS. J Neurol Neurosurg Psychiatry. 2013;84(9):963–8.

49. de Carvalho M, Dengler R, Eisen A, England JD, Kaji R, Kimura J, et al. Electrodiagnostic criteria for diagnosis of ALS. Vol. 119, Clinical Neurophysiology. 2008. p. 497–503.

50. Okita T, Nodera H, Shibuta Y, Nodera A, Asanuma K, Shimatani Y, et al. Can Awaji ALS criteria provide earlier diagnosis than the revised El Escorial criteria? J Neurol Sci. 2011 Mar 15;302(1–2):29–32.

51. Cedarbaum JM, Stambler N. Performance of the Amyotrophic Lateral Sclerosis Functional Rating Scale (ALSFRS) in multicenter clinical trials. Vol. 1, Journal of Neurological Sciences 152 Suppl. 1997.

52. Blijham PJ, Schelhaas HJ, ter Laak HJ, van Engelen BGM, Zwarts MJ. Early diagnosis of ALS: The search for signs of denervation in clinically normal muscles. J Neurol Sci. 2007 Dec 15;263(1–2):154–7.

53. Nakata M, Kuwabara S, Kanai K, Misawa S, Tamura N, Sawai S, et al. Distal excitability changes in motor axons in amyotrophic lateral sclerosis. Clinical Neurophysiology. 2006 Jul;117(7):1444–8.

54. Vucic S, Kiernan MC. Axonal excitability properties in amyotrophic lateral sclerosis. Clinical Neurophysiology. 2006 Jul;117(7):1458–66.

55. Robberecht W, Philips T. The changing scene of amyotrophic lateral sclerosis. Vol. 14, Nature Reviews Neuroscience. 2013. p. 248–64.

56. Van Dyke JM, Smit-Oistad IM, Macrander C, Krakora D, Meyer MG, Suzuki M. Macrophage-mediated inflammation and glial response in the skeletal muscle of a rat model of familial amyotrophic lateral sclerosis (ALS). Exp Neurol. 2016 Mar 1;277:275–82.

57. Chiu IM, Phatnani H, Kuligowski M, Tapia JC, Carrasco MA, Zhang M, et al. Activation of innate and humoral immunity in the peripheral nervous system of ALS transgenic mice. Proc Natl Acad Sci U S A. 2009 Dec 8;106(49):20960–5.

58. Štetkárová I, Ehler E. Diagnostics of Amyotrophic Lateral Sclerosis: Up to Date. Diagnostics. 2021 Feb 1;11(2).

59. De Carvalho M. Electrodiagnosis of Amyotrophic Lateral Sclerosis: A Review of Existing Guidelines. Vol. 37, Journal of Clinical Neurophysiology. Lippincott Williams and Wilkins; 2020. p. 294–8.

60. Liu J, Zhang X, Ding X, Song M, Sui K. Analysis of clinical and electrophysiological characteristics of 150 patients with amyotrophic lateral sclerosis in China. Neurological Sciences. 2019 Feb 1;40(2):363–9.

61. Pradat PF, El Mendili MM. Neuroimaging to investigate multisystem involvement and provide biomarkers in amyotrophic lateral sclerosis. Vol. 2014, BioMed Research International. Hindawi Publishing Corporation; 2014.

62. Wang S, Melhem ER. Amyotrophic lateral sclerosis and primary lateral sclerosis: The role of diffusion tensor imaging and other advanced MR-based techniques as objective upper motor neuron markers. In: Annals of the New York Academy of Sciences. New York Academy of Sciences; 2005. p. 61–77.

63. Misawa S, Noto Y, Shibuya K, Isose S, Sekiguchi Y, Nasu S, et al. Ultrasonographic detection of fasciculations markedly increases diagnostic sensitivity of ALS [Internet]. 2011. Available from: www.neurology.org

64. Lavorato A, Aruta G, De Marco R, Zeppa P, Titolo P, Colonna MR, et al. Traumatic peripheral nerve injuries: a classification proposal. Journal of Orthopaedics and Traumatology. 2023 Dec 1;24(1).

65. Ferrante MA. The Assessment and Management of Peripheral Nerve Trauma. Vol. 20, Current Treatment Options in Neurology. Current Science Inc.; 2018.

66. Sunderland SS. The anatomy and physiology of nerve injury. Muscle Nerve. 1990;13(9):771–84.

67. Sunderland S. The nerve lesion in the carpal tunnel syndrome. Vol. 39, Neurosurgery, and Psychiatry. 1976.

68. Seddon HJ, Nu FRCS. A CLASSIFICATION OF NERVE INJURIES.

69. Robinson LR. Traumatic injury to peripheral nerves. Vol. 23, Muscle and Nerve. 2000. p. 863–73.

70. Sydney Sunderland B. A CLASSIFICATION OF PERIPHERAL NERVE FNJURIES PRODUCING LOSS OF FUNCTION [Internet]. Available from: http://brain.oxfordjournals.org/

71. 13 Mackinnon.

72. Campbell WW. Evaluation and management of peripheral nerve injury. Vol. 119, Clinical Neurophysiology. 2008. p. 1951–65.

73. Symanski JS, Ross AB, Davis KW, Brunner MC, Lee KS. US for Traumatic Nerve Injury, Entrapment Neuropathy, and Imaging-guided Perineural Injection. Radiographics. 2022 Sep 1;42(5):1546–61.

74. Holzgrefe RE, Wagner ER, Singer AD, Daly CA. Imaging of the Peripheral Nerve: Concepts and Future Direction of Magnetic Resonance Neurography and Ultrasound. Vol. 44, Journal of Hand Surgery. W.B. Saunders; 2019. p. 1066–79.

75. Toia F, Gagliardo A, D'Arpa S, Gagliardo C, Gagliardo G, Cordova A. Preoperative evaluation of peripheral nerve injuries: What is the place for ultrasound? J Neurosurg. 2016 Sep 1;125(3):603–14.

76. Brown JM, Yablon CM, Morag Y, Brandon CJ, Jacobson JA. US of the peripheral nerves of the upper extremity: A landmark approach. Radiographics. 2016 Mar 1;36(2):452–63.

77. Agarwal A, Chandra A, Jaipal U, Saini N. A panorama of radial nerve pathologies- an imaging diagnosis: a step ahead. Vol. 9, Insights into Imaging. Springer Verlag; 2018. p. 1021–34.

78. Agarwal A, Chandra A, Jaipal U, Bagarhatta M, Mendiratta K, Goyal A, et al. Can imaging be the new yardstick for diagnosing peripheral neuropathy?—a comparison between high resolution ultrasound and MR neurography with an approach to diagnosis. Insights Imaging. 2019 Dec 1;10(1).

79. Chhabra A, Ahlawat S, Belzberg A, Andreseik G. Peripheral nerve injury grading simplified on MR neurography: As referenced to Seddon and Sunderland classifications. Indian Journal of Radiology and Imaging. 2014;24(3):217–24.

80. Park BK, Hong SH, Jeong WK. Effectiveness of ultrasound in evaluation of fatty infiltration in rotator cuff muscles. CiOS Clinics in Orthopedic Surgery. 2020;12(1):76–85.

81. Noguerol TM, Barousse R, Cabrera MG, Socolovsky M, Bencardino JT, Luna A. Functional MR neurography in evaluation of peripheral nerve trauma and postsurgical assessment. Radiographics. 2019 Mar 1;39(2):427–46.

82. Stoll G, Griffin JW, Li CY, Trapp BD. Wallerian degeneration in the peripheral nervous system: participation of both Schwann cells and macrophages in myelin degradation. Vol. 18, Journal of Neurocytology. 1989.

83. Pellegrino RG, Spencer PS. Schwann Cell Mitosis in Response to Regenerating Peripheral Axons In Vivo. 1985.

84. Funakoshi H, Fris6n J, Barbany G, Timmusk T, Zachrisson O, Verge VMK, et al. Differential Expression of mRNAs for Neurotrophins and Their Receptors after Axotomy of the Sciatic Nerve.

85. Parkinson DB, Bhaskaran A, Arthur-Farraj P, Noon LA, Woodhoo A, Lloyd AC, et al. c-Jun is a negative regulator of myelination. Journal of Cell Biology. 2008 May 19;181(4):625–37.

86. Elfar JC, Jacobson JA, Puzas JE, Rosier RN, Zuscik MJ. Erythropoietin accelerates functional recovery after peripheral nerve injury. Journal of Bone and Joint Surgery. 2008 Aug 1;90(8):1644–53.

87. Vrbova G, Mehra N, Shanmuganathan H, Tyreman N, Schachner M, Gordon T. Chemical communication between regenerating motor axons and Schwann cells in the growth pathway. European Journal of Neuroscience. 2009;30(3):366–75.

88. 52.

89. Birchmeier C, Nave KA. Neuregulin-1, a key axonal signal that drives schwann cell growth and differentiation. Glia. 2008;56(14):1491–7.

90. Menorca RMG, Fussell TS, Elfar JC. Nerve physiology. Mechanisms of injury and recovery. Vol. 29, Hand Clinics. 2013. p. 317–30.

91. Reichert F, Saada A, Rotshenker S. Peripheral Nerve Injury Induces Schwann Cells to Express Two Macrophage Phenotypes: Phagocytosis and the Galactose-Specific Lectin MAC-2. 1994.

92. 62 Taskinen.

93. Toews AD, Barrett C, Morell P. Monocyte chemoattractant protein 1 is responsible for macrophage recruitment following injury to sciatic nerve. J Neurosci Res. 1998 Jul 15;53(2):260–7.

94. Baichwal RR, Bigbeet JW, Devries GH. Macrophage-mediated myelin-related mitogenic factor for cultured Schwann cells (Wailerian degeneration/mitogen/lysosomal processing). Vol. 85, Proc. Natl. Acad. Sci. USA. 1988.

95. Rotshenker S. Microglia and Macrophage Activation and the Regulation of Complement-Receptor-3 (CR3/MAC-1)-Mediated Myelin Phagocytosis in Injury and Disease. 2003.

96. Brück W. The role of macrophages in Wallerian degeneration. Vol. 7, Brain Pathology. Blackwell Publishing Ltd; 1997. p. 741–52.

97. Venezie RD, Toews AD, Morell P. Macrophage recruitment in different models of nerve injury: Lysozyme as a marker for active phagocytosis. J Neurosci Res. 1995;40(1):99–107.

98. Weinberg HJ, Spencer PS. The fate of Schwann cells isolated from axonal contact. Vol. 7, Journal ofNeurocytology. 1978.

99. Peterson TE, Manning HC. Molecular imaging: 18F-FDG PET and a whole lot more. Vol. 37, Journal of Nuclear Medicine Technology. 2009. p. 151–61.

100. Pysz MA, Gambhir SS, Willmann JK. Molecular imaging: current status and emerging strategies. Vol. 65, Clinical Radiology. 2010. p. 500–16.

101. Wu M, Shu J. Multimodal Molecular Imaging: Current Status and Future Directions. Vol. 2018, Contrast Media and Molecular Imaging. Hindawi Limited; 2018.

102. Coda AR, Anzilotti & S, Boscia F, Greco & A, Panico & M, Gargiulo & S, et al. In vivo imaging of CNS microglial activation/macrophage infiltration with combined [18 F]DPA-714-PET and SPIO-MRI in a mouse model of relapsing remitting experimental autoimmune

encephalomyelitis. Eur J Nucl Med Mol Imaging [Internet]. 2021;48:40–52. Available from: https://www.slicer.org

103. Wu C, Yue X, Lang L, Kiesewetter DO, Li F, Zhu Z, et al. Longitudinal PET imaging of muscular inflammation using 18F-DPA-714 and 18F-alfatide II and differentiation with tumors. Theranostics. 2014;4(5):546–55.

104. Stoll G, Bendszus M. Imaging of inflammation in the peripheral and central nervous system by magnetic resonance imaging. Vol. 158, Neuroscience. 2009. p. 1151–60.

105. Ghanouni P, Behera D, Xie J, Chen X, Moseley M, Biswal S. In vivo USPIO magnetic resonance imaging shows that minocycline mitigates macrophage recruitment to a peripheral nerve injury. Mol Pain. 2012 Jun 28;8.

106. Jan YK, Hung IYJ, Cheung WC. Texture Analysis in Musculoskeletal Ultrasonography: A Systematic Review. Vol. 15, Diagnostics. Multidisciplinary Digital Publishing Institute (MDPI); 2025.

107. Noda Y, Sekiguchi K, Matoba S, Suehiro H, Nishida K, Matsumoto R. Real-time artificial intelligence-based texture analysis of muscle ultrasound data for neuromuscular disorder assessment. Clin Neurophysiol Pract. 2024 Jan 1;9:242–8.

108. Cybulska KA, Bloemers V, Perk LR, Laverman P. Optimised GMP-compliant production of [18F]DPA-714 on the Trasis AllinOne module. EJNMMI Radiopharm Chem. 2021 Dec 1;6(1).

109. Neuwelt A, Sidhu N, Hu CAA, Mlady G, Eberhardt SC, Sillerud LO. Iron-based superparamagnetic nanoparticle contrast agents for MRI of infection and inflammation. American Journal of Roentgenology. 2015 Mar 1;204(3):W302–13.

110. Oliván S, Calvo AC, Rando A, Jesús Muñoz M, Zaragoza P, Osta R. Comparative study of behavioural tests in the SOD1G93A mouse model of amyotrophic lateral sclerosis.

111. McCoyd M, Salardini A, Biller J. The Neurological Examination. Operative Neurosurgery. 2019 Aug 1;17:S3–16.

112. Murphy SM, Herrmann DN, McDermott MP, Scherer SS, Shy ME, Reilly MM, et al. Reliability of the CMT neuropathy score (second version) in Charcot-Marie-Tooth disease. Journal of the Peripheral Nervous System. 2011 Sep;16(3):191–8.

113. Graham RC, Hughes RAC. A modified peripheral neuropathy scale: The Overall Neuropathy Limitations Scale. J Neurol Neurosurg Psychiatry. 2006;77(8):973–6.

114. Paternostro-Sluga T, Grim-Stieger M, Posch M, Schuhfried O, Vacariu G, Mittermaier C, et al. Reliability and validity of the Medical Research Council (MRC) scale and a modified scale for testing muscle strength in patients with radial palsy. J Rehabil Med. 2008 Sep;40(8):665–71.

115. Moraux A, Canal A, Ollivier G, Ledoux I, Doppler V, Payan C, et al. Ankle dorsi- and plantar-flexion torques measured by dynamometry in healthy subjects from 5 to 80 years. BMC Musculoskelet Disord. 2013;14.

116. Agarwala P, Salzman SH. Six-Minute Walk Test: Clinical Role, Technique, Coding, and Reimbursement. Vol. 157, Chest. Elsevier Inc; 2020. p. 603–11.

117. Lima CA, Ricci NA, Nogueira EC, Perracini MR. The Berg Balance Scale as a clinical screening tool to predict fall risk in older adults: a systematic review. Vol. 104, Physiotherapy (United Kingdom). Elsevier Ltd; 2018. p. 383–94.

118. Delgado DA, Lambert BS, Boutris N, McCulloch PC, Robbins AB, Moreno MR, et al. Validation of Digital Visual Analog Scale Pain Scoring With a Traditional Paper-based Visual Analog Scale in Adults. J Am Acad Orthop Surg Glob Res Rev. 2018 Mar 1;2(3).

119. Fadli D, Lintingre PF, Dallet L, Raoult J, Gay-Depassier J, Bouguennec N, et al. An Evaluation of Magnetic Resonance Imaging Dixon Sequence Fat–Water Separation Techniques (T2w Dixon FSTs) to Detect Dorso-Lumbar Structural Lesions in Patients with Axial Spondyloarthritis. Bioengineering. 2025 May 1;12(5).

120. Arachchige ASPM, Verma Y. State of the art in the diagnostic evaluation of osteomyelitis: exploring the role of advanced MRI sequences-a narrative review. Vol. 14, Quantitative Imaging in Medicine and Surgery. AME Publishing Company; 2024. p. 1070–85.

121. Beleù A, Canonico D, Morana G. T1 and T2-mapping in pancreatic MRI: Current evidence and future perspectives. Eur J Radiol Open. 2024 Jun 1;12.

122. Heidenreich JF, Weng AM, Donhauser J, Greiser A, Chow K, Nordbeck P, et al. T1- and ECV-mapping in clinical routine at 3 T: Differences between MOLLI, ShMOLLI and SASHA. BMC Med Imaging. 2019 Aug 1;19(1).

123. Haaf P, Garg P, Messroghli DR, Broadbent DA, Greenwood JP, Plein S. Cardiac T1 Mapping and Extracellular Volume (ECV) in clinical practice: A comprehensive review. Vol. 18, Journal of Cardiovascular Magnetic Resonance. BioMed Central Ltd.; 2016.

124. Salerno M, Kramer CM. Advances in parametric mapping with CMR imaging. Vol. 6, JACC: Cardiovascular Imaging. 2013. p. 806–22.

125. Messroghli DR, Moon JC, Ferreira VM, Grosse-Wortmann L, He T, Kellman P, et al. Clinical recommendations for cardiovascular magnetic resonance mapping of T1, T2, T2 and extracellular volume: A consensus statement by the Society for Cardiovascular Magnetic Resonance (SCMR) endorsed by the European Association for Cardiovascular Imaging (EACVI). Vol. 19, Journal of Cardiovascular Magnetic Resonance. BioMed Central Ltd.; 2017.

126. Moon JC, Messroghli DR, Kellman P, Piechnik SK, Robson MD, Ugander M, et al. Myocardial T1 mapping and extracellular volume quantification: A Society for Cardiovascular Magnetic Resonance (SCMR) and CMR Working Group of the European Society of Cardiology consensus statement. Journal of Cardiovascular Magnetic Resonance. 2013;15(1).

127. Schelbert EB, Messroghli DR. State of the art: Clinical applications of cardiac T1 mapping. Vol. 278, Radiology. Radiological Society of North America Inc.; 2016. p. 658–76.

128. Marty B, Coppa B, Carlier PG. Monitoring skeletal muscle chronic fatty degenerations with fast T1-mapping. Eur Radiol. 2018 Nov 1;28(11):4662–8.

129. Beleù A, Canonico D, Morana G. T1 and T2-mapping in pancreatic MRI: Current evidence and future perspectives. Eur J Radiol Open. 2024 Jun 1;12.

130. Thavendiranathan P, Walls M, Giri S, Verhaert D, Rajagopalan S, Moore S, et al. Improved detection of myocardial involvement in acute inflammatory cardiomyopathies using T2 mapping. Circ Cardiovasc Imaging. 2012 Jan;5(1):102–10.

131. O'Brien AT, Gil KE, Varghese J, Simonetti OP, Zareba KM. T2 mapping in myocardial disease: a comprehensive review. Vol. 24, Journal of Cardiovascular Magnetic Resonance. BioMed Central Ltd; 2022.

132. Baeßler B, Schaarschmidt F, Stehning C, Schnackenburg B, Maintz D, Bunck AC. A systematic evaluation of three different cardiac T2-mapping sequences at 1.5 and 3T in healthy volunteers. Eur J Radiol. 2015 Nov 1;84(11):2161–70.

133. Usman AA, Taimen K, Wasielewski M, McDonald J, Shah S, Giri S, et al. Cardiac magnetic resonance T2 mapping in the monitoring and follow-up of acute cardiac transplant rejection: A pilot study. Circ Cardiovasc Imaging. 2012 Nov;5(6):782–90.

134. Kim PK, Hong YJ, Im DJ, Suh YJ, Park CH, Kim JY, et al. Myocardial T1 and T2 mapping: Techniques and clinical applications. Vol. 18, Korean Journal of Radiology. Korean Radiological Society; 2017. p. 113–31.

135. Sprinkart AM, Luetkens JA, Träber F, Doerner J, Gieseke J, Schnackenburg B, et al. Gradient Spin Echo (GraSE) imaging for fast myocardial T2 mapping. Journal of Cardiovascular Magnetic Resonance. 2015 Feb 3;17(1).

136. Atif M, Alsayyad I, Ghafar AA, Mohamed B, Shehata KAA, Khattab RT. ROLE OF MRI T2 MAPPING IN ASSESSMENT OF ARTICULAR KNEE CARTILAGE IN OSTEOARTHRITIS. Vol. 71, AIN SHAMS MEDICAL JOURNAL. 2020.

137. Noguerol TM, Barousse R, Cabrera MG, Socolovsky M, Bencardino JT, Luna A. Functional MR neurography in evaluation of peripheral nerve trauma and postsurgical assessment. Radiographics. 2019 Mar 1;39(2):427–46.

138. Ferrante MA. The Assessment and Management of Peripheral Nerve Trauma. Vol. 20, Current Treatment Options in Neurology. Current Science Inc.; 2018.

139. Holzgrefe RE, Wagner ER, Singer AD, Daly CA. Imaging of the Peripheral Nerve: Concepts and Future Direction of Magnetic Resonance Neurography and Ultrasound. Vol. 44, Journal of Hand Surgery. W.B. Saunders; 2019. p. 1066–79.

140. Eppenberger P, Andreisek G, Chhabra A. Magnetic resonance neurography. Diffusion tensor imaging and future directions. Vol. 24, Neuroimaging Clinics of North America. 2014. p. 245–56.

141. Zhou Y, Narayana PA, Kumaravel M, Athar P, Patel VS, Sheikh KA. High resolution diffusion tensor imaging of human nerves in forearm. Journal of Magnetic Resonance Imaging. 2014;39(6):1374–83.

142. Bruno F, Arrigoni F, Mariani S, Patriarca L, Palumbo P, Natella R, et al. Application of diffusion tensor imaging (DTI) and MR-tractography in the evaluation of peripheral nerve tumours: State of the art and review of the literature. Vol. 90, Acta Biomedica. Mattioli 1885; 2019. p. 68–76.

143. DISABILITIES OF THE ARM, SHOULDER AND HAND DA SH.

144. Sereda M, Griffiths I, Pü hlhofer A, Stewart H, Rossner MJ, Zimmermann F, et al. A Transgenic Rat Model of Charcot-Marie-Tooth Disease. Vol. 16, Neuron. Snipes and Suter; 1049.

145. Bendszus M, Stoll G. Cellular/Molecular Caught in the Act: In Vivo Mapping of Macrophage Infiltration in Nerve Injury by Magnetic Resonance Imaging. 2003.

146. Lupski JR, Montes De Oca-Luna R, Slaugenhaupt S, Pentao L, Guzzetta V, Trask BJ, et al. DNA Duplication Associated with Charcot-Marie-Tooth Disease Type 1 A. Vol. 66, Cell. 1991.

147. Klein D, Gnes Patzkó A´, Schreiber D, Van Hauwermeiren A, Baier M, Groh J, et al. Targeting the colony stimulating factor 1 receptor alleviates two forms of Charcot-Marie-Tooth disease in mice. Available from: http://brain.oxfordjournals.org/

148. Klein D, Groh J, Weishaupt A, Martini R. Endogenous antibodies contribute to macrophage-mediated demyelination in a mouse model for CMT1B. J Neuroinflammation. 2015 Dec 12;12(1).

149. Shefner JM, Musaro A, Ngo ST, Lunetta C, Steyn FJ, Robitaille R, et al. Skeletal muscle in amyotrophic lateral sclerosis. Vol. 146, Brain. Oxford University Press; 2023. p. 4425–36.

150. Marini C, Riondato M, Dighero E, Democrito A, Losacco S, Emionite L, et al. Increased [18F]DPA-714 Uptake in the Skeletal Muscle of SOD1G93A Mice: A New Potential of Translocator Protein 18 kDa Imaging in Amyotrophic Lateral Sclerosis. Biomolecules. 2025 Jun 1;15(6).